Laser-Based Imaging of Novel Charge Density Wave and Superconducting Materials

by

Tarun Patel

A thesis
presented to the University of Waterloo
in fulfillment of the
thesis requirement for the degree of
Doctor of Philosophy
in
Physics(Quantum Information)

Waterloo, Ontario, Canada, 2021

Examining Committee Membership

The following served on the Examining Committee for this thesis. The decision of the Examining Committee is by majority vote.

External Examiner:	Jayakanth Ravichandran Assistant Professor, Dept. of Chemical Engineering and Materials Science, University of Southern California
Supervisor(s):	Adam Wei Tsen Assistant Professor, Dept. of Chemistry, University of Waterloo
Internal Member:	David Hawthorn Professor, Dept. of Physics and Astronomy, University of Waterloo
Internal-External Member:	Michael Reimer Assistant Professor, Dept. of Electrical and Computer Engineering, University of Waterloo
Internal-External Member:	Germán Sciaini Associate Professor, Dept. of Chemistry, University of Waterloo

Author's Declaration

This thesis consists of material all of which I authored or co-authored: see Statement of Contributions included in the thesis. This is a true copy of the thesis, including any required final revisions, as accepted by my examiners.

I understand that my thesis may be made electronically available to the public.

Statement of Contributions

The work presented in this thesis would not have been possible without help of my co-workers and collaborators.

The transfer stage used for fabricating Van-der-Waals heterostructure was designed and setup by Prof. Adam Wei Tsen and Daniel McHaffie. Hyun Ho Kim and Bowen Yang developed and improved the fabrication techniques for these samples. Tina Dekker fabricated some of the heterostructure samples. 1T-TaS_2 crystals were grown in China by Jingjing Gao, Xuan Luo, Wenjian Lu in the group led by Prof. Yuping Sun. The optics setup was designed by Bowen Yang, me and Prof. Adam Wei Tsen. It was later setup by me. Au/Ti electrodes were fabricated in QNFCF clean-room with help of Archana Tiwari, Shazhou Zhong and Hyun Ho Kim. Dr. Junichi Okamoto developed the phenomenological model of the multi-step electrically driven transition seen in our devices.

Prof. Tom Timusk designed the high pressure hydride experiment. He also arranged for the high-pressure samples which were fabricated in Germany by the team led by Prof. Mikhail Eremets. The first holder for these samples were designed by me and fabricated by Alex Mitrovic.

- Chapter 4 is adapted from our publication:

  Tarun Patel, Junichi Okamoto, Tina Dekker, Bowen Yang, Jingjing Gao, Xuan Luo, Wenjian Lu, Yuping Sun, and Adam W. Tsen, "Photocurrent Imaging of Multi-Memristive Charge Density Wave Switching in Two-Dimensional 1T-TaS_2" *Nano Letters* 2020 20 (10), 7200-7206 , DOI: 10.1021/acs.nanolett.0c02537

Abstract

The following thesis presents experimental study of two crystalline materials which show correlated electron phases.

The first material 1T-TaS_2 is a two-dimensional van-der-Waals material. This family of materials have been of intense research interest since the discovery of mechanical exfoliation technique, which allows for fabrication of atomically thin flakes of high crystal quality. Subsequent development in dry-transfer techniques have created the capacity to vertically stack these flakes to get desired heterostructures. Bulk crystals of 1T-TaS_2 had been previously studied and were known to undergo multiple charge density waves (CDW) transitions as a function of temperature. In ultra-thin flakes of 1T-TaS_2 the temperature hysteresis of Nearly-Commensurate (NC) to Commensurate (C) phase transition has been shown to widen and host states of intermediate resistivity. While such measurements provide global information, a spatially resolved study would answer the question of distribution of the NC-C phases in these states. Such a study would help to identify further differences between these intermediate states and also answer questions relevant for device miniaturization. In order to achieve this, we propose a vertical heterostructure geometry of the following order h-BN/1T-TaS_2/WSe_2/Gr. This geometry utilizes the high photocurrent extraction efficiency of such devices to map the phase of 1T-TaS_2 in the overlap region. A scanning laser microscopy system is used to map the photocurrent response of these devices with diffraction limited resolution. We compare the spatial maps obtained for such devices with relatively thick and thin 1T-TaS_2 flakes as they undergo the NC-C phase transitions. Further motivation to study this material is for its potential use in electronic devices. Various methods have been shown to alter the phase of the material over a wide temperature range. Applied electric field has been previously shown to control the CDW state of the ultra-thin flakes by driving the material from the NC to C or C to NC state in a unidirectional manner. We are able to reproduce this control and additionally able to achieve bi-directional driving at a constant temperature. Spatial photocurrent maps of such control provide additional information which is modeled phenomenologically by a free

energy analysis.

The second class of materials we study are high pressure Hydrides which are known to have the highest superconducting T_C. Metallic hydrogen was first proposed to be a room temperature superconductor by Ashcroft in 1968, but the high pressure requirement to fabricate such material still remains beyond practical limit. Alternatively it was suggested that hydrogen dense compounds could harbor high-temperature superconductivity at more achievable pressures . H_3S and LaH_{10} are two such materials that show superconductivity at 203K and 250K respectively. While it is possible to measure electrical resistivity of these samples, it is difficult to measure other properties of superconductivity like the Meissner effect as the samples are held at high pressures under diamond anvils. Optical measurements that consider the presence of diamond in the beam path offer the possibility of exploring the nature of superconductivity in these exotic samples. Previous measurements exploring the reflectivity of H_3S superconducting samples in the near-infrared regime show a dip in the 400-650meV energy range. This matches with theoretical predictions that assign this depression of reflectance to strong scattering from bosonic excitations. We aim to use this result to spatially map the superconductivity in these samples using our laser scanning setup with laser wavelength of 2300nm. In this thesis we report the initial data taken on a H_3S sample.

Acknowledgements

I would like to thank all the people without whom the research presented in this thesis and this thesis would not have possible. First of all is Dr. Adam Wei Tsen who welcomed me to his new group to setup the optics lab which was just an empty room when I arrived. He also guided the design of the heterostructure project and provided me with the experimental tools that showed it the light of day. In addition to his active interest in helping on the experimental front I deeply appreciate his help in making my research presentable and clarifying my often rambling thoughts. Special thanks to the people who developed the fabrication techniques that I could reliably follow, these include Hyun Ho Kim, Bowen Yang and Archana Tiwari. I am grateful to Tina Dekker making the samples that kept the measurements going when fabrication was getting difficult. I would also like to thank Shazhou Zhong who has been managing to keep our data backed up.

Outside our group I am thankful of our collaborators in China under Dr. Yuping Sun's group who grew the 1T-TaS_2 crystals. Dr. Junichi Okamoto holds a special place for doing the theory on my results and also helping in the draft preparation of our publication. I am extremely thankful of Prof. Tom Timusk who designed and guided the hydride project. His deep knowledge of condensed matter physics kept me motivated and fresh in my outlook towards research. I am thankful towards Dr. Vasily Minkov and Prof. Mikhail Eremets who sent us the fresh H_3S samples that were used for the results presented in the thesis. I would also like to mention Prof. Sciaini and Prof. Reimer from whose labs I continue to exchange instruments and knowledge from.

I would like to mention my roommates over this journey who kept me company far away from home. In no particular order they are Akanksha, Babar, Neha, Chathura,Sid and Edward. Vinnie and Nessy hold a special place for being the most hospitable people I have known.

And last but the most important of all are my parents and my brother who in spite of our acrimonious banter kept and keep supporting me through all of my various travels. A

special mention for a new addition to that group, my sister-in-law who has adapted quite well to our madness.

Dedication

To Ms.Athena and Saraswati.

And

My grandparents who passed away due to the COVID-19 pandemic.

Table of Contents

List of Figures

Chapter 1

Introduction

Phase transitions that originate from non-trivial electronic order are interesting to investigate from both physics and device application point of view. One type of such an order can cause metal-insulator transition materials susceptible to Charge Density Wave (CDW) ordering. Alternatively, if electrons pair together they can condense to the same quantum ground state and give rise to superconductivity. In this thesis we use light in the visible and near-infrared (IR) spectrum to spatially map such phase transitions in different material systems. For the CDW material we show control of the phase transition by changing the thickness of the material and applying an external electric field. The spatial mapping reveals important differences between intermediate states obtained upon thermal and electrically driven transitions. The superconducting material we study is fabricated and held at extremely high pressures which makes measurement of it's physical properties challenging. Our experiment intends to use the change of the reflection spectrum in the near-IR region to spatially map the inhomogeneity of superconductivity in the sample.

We assemble a scanning laser microscopy setup to achieve our spatial mapping which is limited by the diffraction limit of the incident light. In Chapter 2, covering experimental techniques we present the design of this setup, which is coupled to a cryostat with electrical contact leads that allow for simultaneous electronic measurements. This chapter also covers

the device fabrication technique that is used to thin down and assemble nano-meter (nm) thin 2D Van der Waals heretostructures that is used to fabricate samples of the CDW material.

The CDW material studied is 1T-TaS_2 which is know to harbor multiple CDW phases. An overview of previous work done on these phases in the bulk crystal is presented in Chapter 3. Recent work on thinning this material down to the nm limit is also presented in the same chapter. Previous results from these ultra-thin flakes motivate spatial mapping of the Nearly-Commensurate (NC) - Commensurate (C) CDW phase transition.

In Chapter 4 we present a device geometry involving a vertically stacked van der Waals heterostructure that would enable us to do such spatial mapping using photocurrent microscopy. The proposed geometry additionally allows for electrical driving of the NC-C CDW phases. We present the photo-current maps obtained from such devices where the phase transition takes place either due to thermal cycling or an applied electric field. These maps show important differences between both processes. The results obtained for electrically driven transitions are unique as they achieve bi-directional electrical control over the phase transition at a constant temperature. A phenomenological model for the electrically driven step-wise transition from the NC to C phase is presented at the end of the chapter.

Chapter 5 deals with the reflection based scanning microscopy of high pressure Hydride systems. These materials are currently contending to have the highest known T_C for a superconductor. Theoretical calculations predict a change in reflectivity of these samples in the near infra-red region due to the superconducting transition. We design an experiment by choosing a laser with wavelength in this spectral region and present initial laser scanning reflection images taken on superconducting H_3S.

1.1 Charge Density Waves

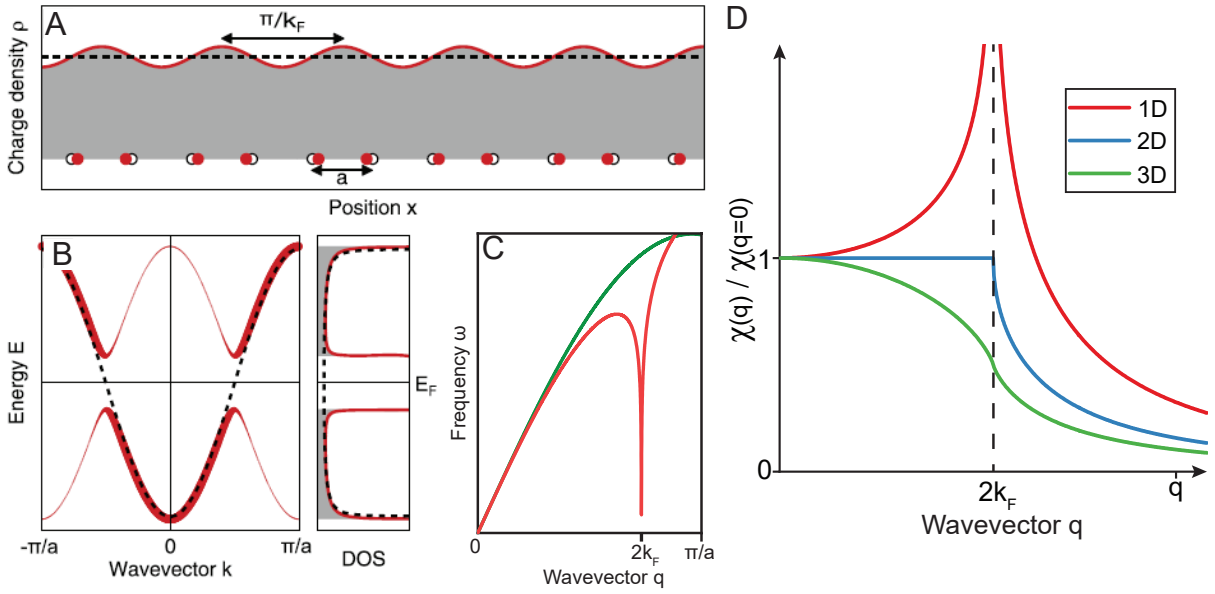

Figure 1.1: Instability of a 1D half-filled band and the formation of CDW order. (A) The regular lattice of equally spaced ions (black circles) and uniformly distributed charge density (black dashed line) rearranges to create a CDW (solid red line) and distorts the underlying lattice (red dots).(B) Formation of the CDW opens a band gap (solid red line) at the Fermi energy in the metallic band (dashed black line). This change in density of states (DOS) is shown in the right panel. (C) The energy of the acoustic phonon mode at twice the Fermi wave-vector goes to zero indicating the formation of a static lattice distortion. (D) Lindhard response function for 1D, 2D, 3D free electron gas at zero temperature. A 1D electron gas has a diverging response at the Fermi wavevector.Figure (A), (B) taken from [49]

The instability of a 1D crystal with a half filled electron band was first discussed by Peierls. [45] This instability causes a regularly spaced lattice and a uniformly distributed

electron gas to develop a periodic lattice distortion (PLD) and a periodically varying charge modulation with a wavelength $\lambda_0 = \pi/k_F$ (Fig 1.1(A)) where k_F is the Fermi wavevector. The lattice distortion leads to a single particle gap at the Fermi level (Fig 1.1(B)) inducing a metal-to-insulator transition in the material. The instability of this system is attributed to the divergent behavior of the wavelength dependent dielectric function for a 1D electron gas as shown in Fig 1.1(D). The y-axis plots the Lindhard response function [21], which maps the wavevector dependent response of an electron gas to a time independent potential for 1D , 2D and 3D electron gas. The divergence of the response function at $2k_F$ is due to the topology of the Fermi surface of a 1D electron gas called perfect nesting [21]. Since the transition primarily addresses a reduction in the kinetic energy by damping the scattering at the Fermi wavevector the PLD is in general incommensurate with the underlying crystal lattice[49]. As a consequence of the lattice distortion the phonon mode at $2k_F$ is greatly suppressed (Fig 1.1(C)), and is generally referred to as the Kohn anomaly [29]. It was independently suggested by Fröhlich that the ground state of this system can carry an electric current [19] under the influence of an applied electric field. This formulation of CDW for a 1D crystal can be directly used to understand CDW in quasi-1D materials such as $NbSe_3$ [60].

In this thesis we work with a quasi-2D crystal with a much more complex CDW ordering, where the dominant CDW modulation is in the 2D plane described by 3 symmetric 1D-CDW wavevectors. Many members of 2-D MX_2 (M = metal, X = chalcogenide) family of transition-metal dichalcogenides show these CDW phases. Such as 1T-TaS_2, 2H-$TaSe_2$,1T-$TiSe_2$ [72] and more. We focus our work on 1T-TaS_2 which has a rich phase diagram and is the only member of the Tantalum dichalcogenide family to undergo a complete metal-to-insulator transition. It has a $\sqrt{13}\times\sqrt{13}$ CDW/PLD in-plane superstructure. Upon cooling from 560K to 352K the CDW is incommensurate (IC), between 352K and 180K the CDW is Nearly-commensurate(NC) and from 180K onward the CDW is commensurate with the underlying lattice. Upon warming there is a large thermal hysteresis between the NC and the C phase as the material comes back to the NC phase around 220K. As it is shown in Chapter 3 thinning of the material widens this hysteresis thus motivating the study of

the spatial evolution of the phase transition. Mapping this evolution and its control using applied electrical field is the major topic of study in this thesis.

1.2 Superconductivity

A superconductor is a material which shows zero-resistance to electric current below a transition temperature T_C. It was discovered in 1911 by H. Kamerlingh Onnes in elemental metals such as mercury, lead and tin at cryogenic temperatures [61]. In addition to it's zero resistance property these materials also exhibit perfect diamagnetism which is famously known as the Meissner effect. Till 1986 the T_C for all known superconductors was below 30K until a separate class of superconductors called Cuprate superconductors [4] were discovered. The T_C value for these copper-based materials has been reported as high as 164K [50]. The search for higher T_C superconductors remains an open field of research.

Atomic Hydrogen at the extreme pressure of 500GPa was predicted by Ashcroft to be superconducting well above room-temperature at around 300-350K.[1] The search for high-temperature superconductivity has been consequently done using BCS theory in Migdal-Eliashberg formulation which targets materials with high hydrogen density. Since such a high pressure is not achievable through current technologies attention has shifted to hydrogen rich compounds[2] such as H_3S[32], LaH_{10}[69][46] where the required pressure below 200GPa is achievable using diamond anvil cells (DAC). It has been shown that these materials have the characteristic sharp drop to zero-resistance near the expected superconducting transition temperature, T_C. But further measurements are limited due to confinement of the samples within the DAC. Making use of transmissivity of diamond it is possible to study the spectroscopic behavior of these materials. It has been predicted using Eliashberg theory that these materials should have a drop in reflectivity after the superconducting phase transition for light in near-infrared spectrum. This drop has been experimentally measured [10] on superconducting H_3S samples using Fourier Transform Infra-Red (FTIR) spectroscopy. We aim to further this result by using this drop to spatially

map the superconducting transition and help identify the distribution of superconductive material in these in-homogeneous samples.

Chapter 2

Experimental Techniques

This chapter details the main experimental techniques used in this thesis. A laser scanning microscope setup is used to study both the material systems. The design of the system was motivated from chapter 4 of [57] which gives much of the relevant information for building and modifying such setups. The first section of this chapter gives a brief description of this design and later details the in-lab setup that can be used for visible and IR laser scanning purposes. The second section shows the mechanical exfoliation process that was used to obtain nano-meter thin flakes of 2-D materials, it is followed by the dry-pick up method that was used to assemble the Van der Waals heterostructre. This process was used to fabricate 1T-TaS_2 samples presented in Chapter 3.

2.1 Scanning Laser Microscopy

A laser is a special source of light as it emits light which is coherent. This coherence is usually measured for lasers in terms of spatial and temporal coherence. Spatial coherence implies that the light emitted form a laser can travel large distances with very low divergence and also allows for the light to be focused to a tight spot. Temporal coherence implies that light emitted from a laser source can have a very narrow spectrum. In such

a case a tight laser spot is limited by the diffraction limit set by the wavelength that the laser emits. A confocal laser scanning microscope (CLSM) uses these properties in combination with principles of scanning confocal microscopy to raster a diffraction limited spot (depending on objective lens) on a given focal plane.

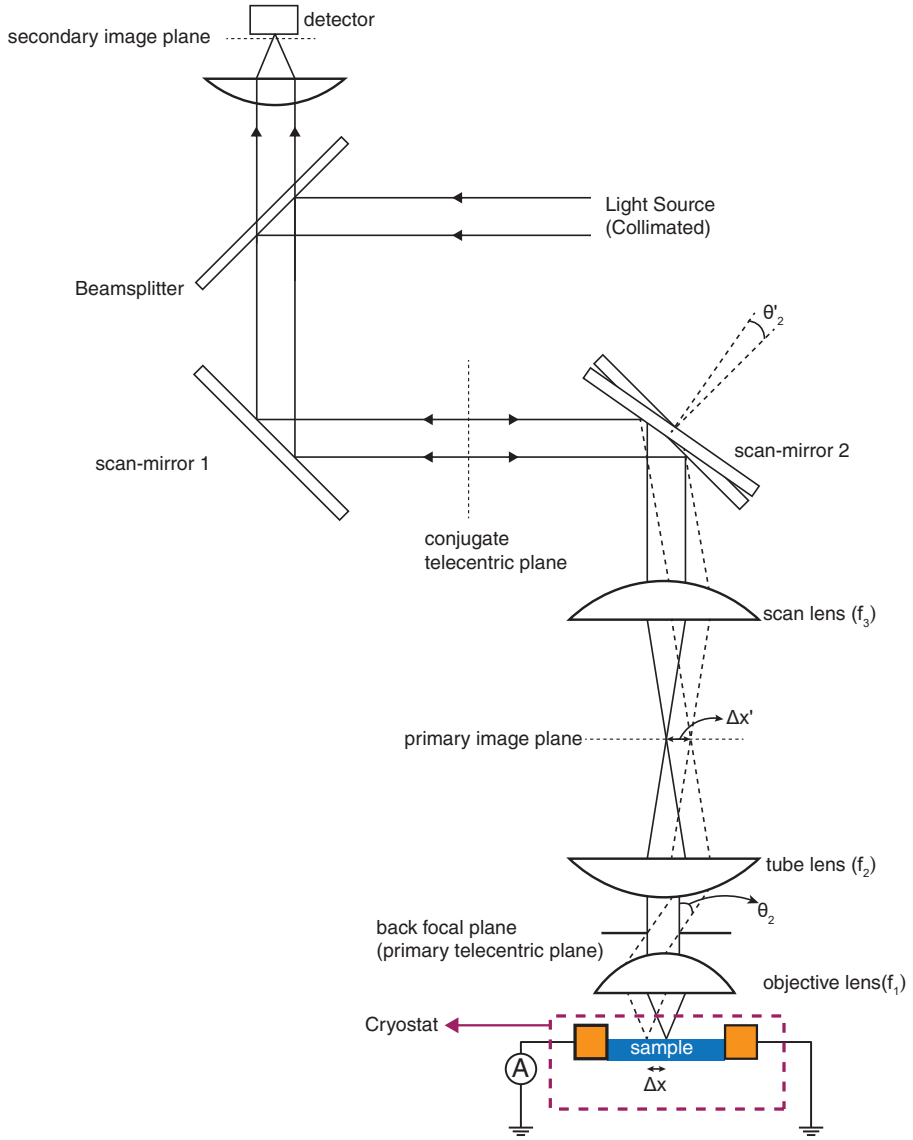

Figure 2.1: Simplified diagram of the components of the scanning laser microscope setup. The microscope objective focuses onto a electrically contacted sample inside a cryostat that works between the temperature range of 4-350K.

In this thesis we use a lab assembled CLSM setup coupled with a Montana C2 cryostat

to measure both the material systems. A schematic of the working components of our system is presented in Fig. 2.1

Collimated laser light is incident on a beamsplitter that allows for collection of the reflected light propagating backwards from the sample. The incident light then shines on a pair of galvo-scanning mirrors whose angle can be controlled using an applied voltage. The beam is then incident on a pair of lenses called the scan lens and tube lens with focal lengths f_3 and f_2 respectively. These lenses are physically separated by a distance of $f_3 + f_2$ which ensures that the light emitted from the tube lens is still collimated. This light is then incident on an objective lens whose back focal plane lies at the focal plane of the tube lens. The objective lens focuses the beam onto the sample. The reflected image of this optical setup is first formed by the combination of the objective and the tube lens at the primary image plane (Fig. 2.1). Thus the first image of our diffraction limited spot is obtained with a magnification of $M = f_2/f_1$. If the back focal length of the objective lens is ∞ then the reflected beam should have similar collimation by the time it passes the conjugate telecentric plane which is the recreation of the back focal plane of the objective. The beamsplitter then allows for collection of the reflected light which is detected using an appropriate detector.

The beam steering is achieved by controlling the angles of the two scan mirrors using a digital-analog signal converter controlled using a computer system. For the sake of simplicity only mirror 2 is shown moving in Fig. 2.1. When the angle of the mirror is changed by θ_2' the angle of the beam incident on the objective lens should change by θ_2. This changes the position of the spot in the focal plane of the objective by $\Delta x = f_1 * \tan(\theta_2)$. This change in position is also reflected in the primary image plane as $\Delta x' = \Delta x * M$.

The selection of lenses for the setup is determined by physical space constraints and the wavelength of light being used. Additionally it is important to get the ratio of f_2/f_3 correct with regards to the beam size as the minimum spot size is obtained by full use of the numerical aperture (NA) of the objective. This happens only when the whole back aperture of the lens is illuminated.

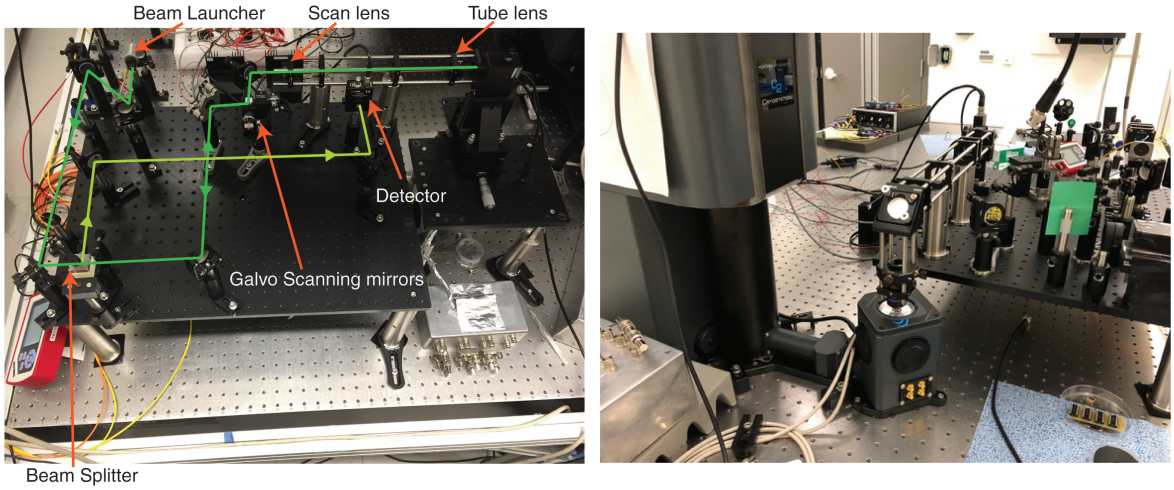

Figure 2.2: CLSM setup based on schematics shown in Fig. 2.1. The picture on the left shows the incident optical path in dark green. The reflected beam path after the beamsplitter is in light green. The objective lens is not visible. The picture on the right shows the setup over the C2 cryostat. Low working distance window allows the objective to focus onto the sample at temperatures down to 4K.

The setup used in this thesis has been designed to accommodate mainly for two wavelength : $\lambda = 520$nm and $\lambda = 2300$nm. Separate laser diodes were used in each case to generate the given wavelength of light. Since the spatial profile of the emitted light were not Gaussian they were coupled into a single mode fiber which only transmits a Gaussian profile. It also allows us to use the same launcher(silver parabolic mirror) for both the wavelengths. The alignment optics used can be seen in Fig. 2.2.

For $\lambda = 520$nm (green) light we used standard lenses with $f_3 = f_2 = 150$mm since the default beam size of the launcher works out with the microscope objective used. The microscope objective used was a transmission based 50x objective with NA = 0.50 and a focal distance of 8mm. The sample was mounted inside a Montana C2 cryostat with a low working distance window that allows the sample to be in the objective focal plane in the

temperature range of 4 - 350K (See Fig. 2.2).

For λ = 2300nm which is in the near IR spectrum CaF_2 lenses have to be used as scan and tube lens. Additionally a reflection based 15x objective lens with NA = 0.50 was used to get a larger working distance (23.2mm). This enables focusing onto the hydride samples which are roughly 10mm deep inside the DAC. Focal lengths of f_3 = 75mm and f_2 = 250mm were chosen to expand the beam such that it completely illuminates the small mirror of the lens.

2.2 2-D Van-der Waals Heterostrcutures

2.2.1 Exfoliation

Scotch-tape (adhesive tapes) exfoliation has become an ubiquitous method of obtaining atomically thin flakes of 2-D Van-der-Waals materials since the discovery of graphene [41] in 2004. Since then it has been used to exfoliate a variety of materials [42] four of which are used in our devices namely: few-layer-graphite(FLG),Tungsten diselenide (WSe_2), 1T-Tantalum(IV) sulfide (1T-TaS_2) and hexagonal Boron nitride (h-BN).

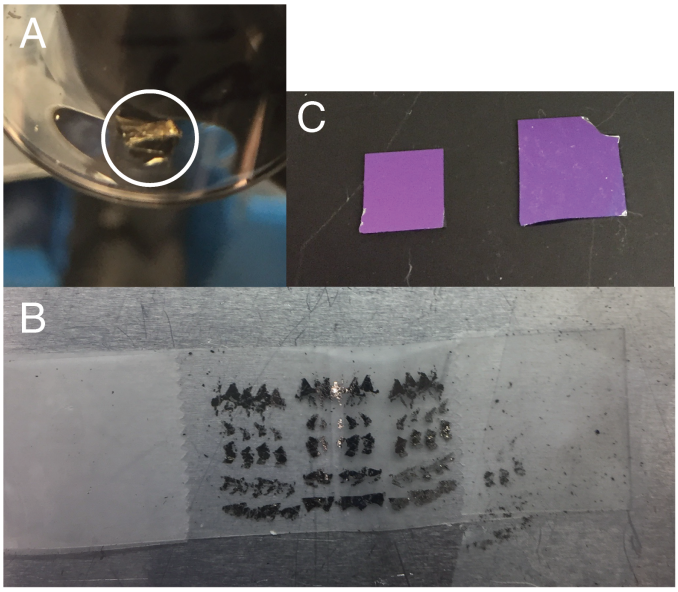

Figure 2.3: Exfoliation technique used to obtain thin flakes (down to the single atom limit) of 2D materials. (A) Bulk 1T-TaS_2 crystal. (B) Bulk crystal is exfoliated multiple times onto a scotch tape inside a N_2 filled glovebox. (C) SiO_2/Si is a commonly used substrate for final exfoliation. The chip on the right is pristine while the left chip has exfoliated crystal on it.

Fig. 2.3 (A) shows a bulk 1T-TaS_2 crystal. It has a characteristic metallic-golden color. Representative of 2-D Van-der-Waals materials the bulk crystals are flat to begin with. Since many 2-D materials including 1T-TaS_2, are sensitive to ambient atmosphere and known to oxidize almost all the exfoliation is carried out in a nitrogen filled glove box (Inert Pure LabHe, P_{O_2},$P_{H_2O} < 0.1$ ppm). [28] [64] For exfoliation a small bulk piece is placed on a scotch tape and the remainder of the tape is folded and peeled over the crystal. The intra-layer Van-der-Waals bonding is a weak bond and thus the crystal peels easily. This process is repeated till the crystal is thinned to a desired thickness.(For 1T-TaS_2 see Fig. 2.3(B)). The tape is then pasted over the desired substrate. Substrates used in this thesis are either SiO_2(280 nm)/Si chips or poly-propylene carbonate(PPC) spin coated

onto a glass slide. Fig. 2.3(C) shows a typical exfoliation onto a SiO_2/Si substrate. The chip on the left is a clean chip which has been cleaved to an appropriate size of around 1cm $\times$ 1cm. The cleaning process involved washing with Acetone and Iso-propanol(IPA) and then a 30min bake in ambient atmosphere at 150-180°C. A chip with exfoliated crystal is shown on the right. The size of the nano-meter thin flakes is usually around $\sim 10\mu$m and are imaged and identified using a regular optical microscope. Fig. 2.4(B) shows two such identified flakes which are then stacked vertically using a polymer baser technique elaborated in the next chapter.

2.2.2 Polymer based transfer techniques.

Once the flakes are exfoliated they are identified under a microscope with magnification upto 100x. Fig. 2.4(A) shows the microscope inside the glove-box with attachments required for fabrication of vertical hetero-structures. The color of the flakes under the mircoscope is related with the thickness of SiO_2 [5], which is comparable to the wavelength of visible light. We choose a thickness of 280nm which maximizes the contrast for thinner flakes which are highly transmissive and thus difficult to locate under the reflection geometry.

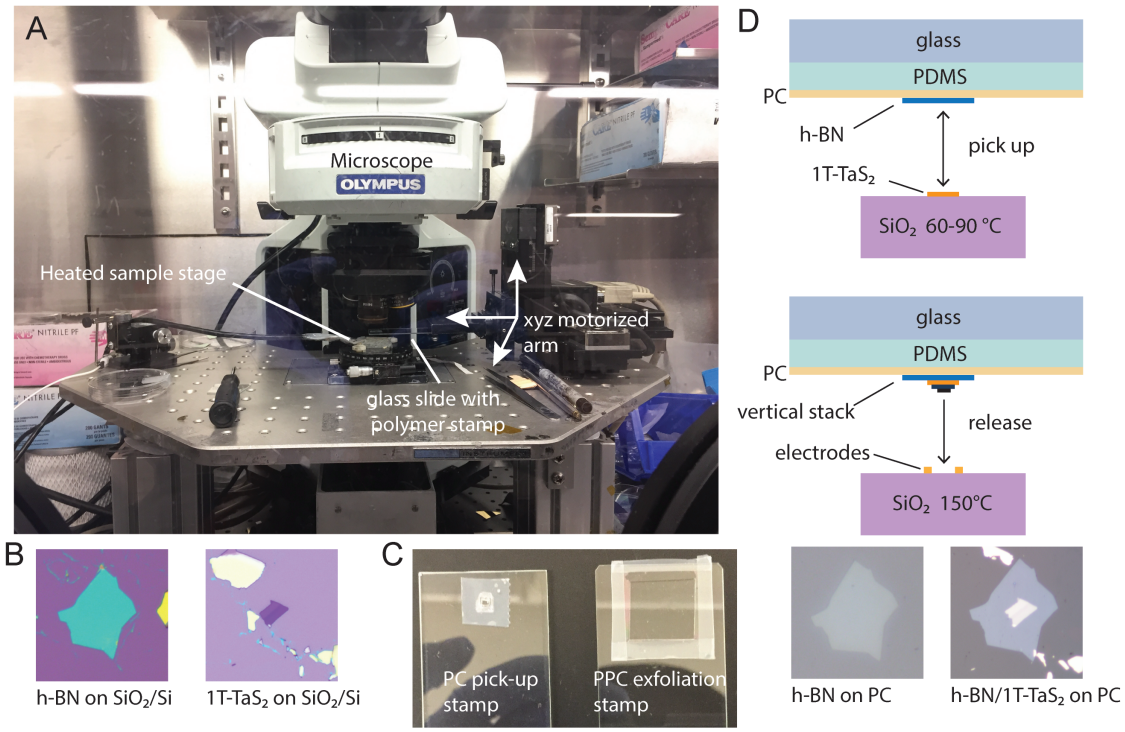

Figure 2.4: Van-der-Waals heterostructure assembly. (A) The assembly setup consists of a reflection microscope with a heated sample stage and a x-y-z controlled motorized arm on which a glass slide can be attached. The microscope is used to identify and select flakes like the ones shown in (B). They are picked using a PC/PDMS stamp an example of which is shown on the left glass slide in (C).(D) Shows the schematic of the pick-up and release process(top). Optical images of sequential pick-up using this method, of flakes shown in (B) is shown in (D)(bottom).

For a fixed SiO_2 thickness the color of flakes observed at a given illumination and exposure time can be correlated with the flake thickness which can be determined using an Atomic force Microscope. For flakes sensitive to air a protective h-BN layer is transferred on top before removal form the glove-box. Once the flake thickness is determined flakes of appropriate thickness and shape are selected for a required hetero-structure. Fig. 2.4(B)

shows a h-BN flake (left) and a 1T-TaS_2(right) (t ∼5-8nm) that have been selected for fabrication of a device with geometry presented in Chapter 4.

A polycarbonate(PC) thin film is created by dripping a PC solution (6% by vol dissolved in chloroform) onto a glass slide and then spread by a second slide put directly over the first slide spreading out the PC. After this the two slides are immediately separated by sliding the two slides over each other. The PC film is then left to dry and harden in air for around 15-30 min. A piece of PC film ∼ 5mm × 5mm is then cut and transferred onto a window made in a relatively piece of scotch tape. This window is then placed onto a ∼ 3mm × 3mm × 1mm piece of polydimethylsiloxane (PDMS) sitting at one end of a glass slide. The process of fabricating hetero-structures involves sequential pick of the crystal flakes using this PC stamp.[78] An example of a PC stamp created in the lab is shown in Fig. 2.4(C) (left)

The glass slide with the stamp is then attached to a x-y-z movable arm near the sample stage. This arm is controlled from outside the glove box and is used to align the stamp over SiO_2/Si chips in order to achieve the required geometry. The sample stage is attached to a heater that can raise the temperature up to 150°C. For picking up flakes using the PC stamp the PC film is gradually brought into contact with the flake. The temperature is then raised between 60-90°C depending on the target material to allow the PC film to relax and conform to the flake. The temperature is then lowered to harden the PC before the stamp is lifted in a continuous manner to pick up the flake without introducing unwanted creases. The bottom-left panel in Fig. 2.4(D) shows an h-BN flake that has been picked using this method. Subsequent flakes for the device can picked in a similar manner. Since 2-D materials adhere better to each other than the underlying SiO_2 they are easily stacked. The top panel of Fig. 2.4(D) shows a schematic of the pick up of a 1T-TaS_2 flake using a h-BN flake using the method described. The bottom right panel shows a 1T-TaS_2 flake picked onto the previously picked up h-BN flake. This process is repeated till the desired stack has been made.

To make electrical contact to the samples we fabricate Au(40nm)/Ti(5nm) electrodes in

a class 100 clean room. Electrodes are patterned on the SiO_2(280 nm)/Si chips either using e-beam lithography with a PMMA A6 resist with writing done using a RAITH 150TWO 30kV Direct Write system or photo-lithography where the writing is done using Heidelberg MLA 150 Direct Write UV lithography system with a Shipley positive resist. After writing, the resist is developed in the appropriate developer solution which exposes the electrode region for the next step. Physical vapor deposition using e-beam heating is used to deposit the metals in a Intlvac-Nanochrome II. The resist is then dissolved in the PG-remover to lift off the excess metal and the chip is cleaved to obtain individual set of electrodes.

The vertical stack is aligned with the electrodes and brought carefully into contact. The temperature is raised to 150 °C to de-laminate the PC in contact with the chip from the PDMS. The glass slide is lifted to release the stack with the PC onto the electrodes. The sample is then put under a vacuum for 10 min and then washed with chloroform to remove the PC layer.

Alternative to the PC pick-up method the crystal flakes can be exfoliated directly onto a PPC film. A PPC solution is made by dissolving it in chloroform (15% by mass) and is then spin-coated onto a cover-glass (30 sec, 1600 RPM). The glass is then heated at 85°C with PPC side up to remove all chloroform from the PC film. After this a window is made around the PC film using tape and then flakes are exfoliated onto the film using a tape similar to the one shown in Fig. 2.3 (B). The tape is then used to peel off the PPC window from the glass substrate which is then placed onto a PDMS stamp $\sim$ 1.5cm $\times$ 1.5cm $\times$ 1mm. An example of such a stamp is shown in Fig. 2.4(C)(right). The glass slide is then attached to the motorized arm in the glove-box transfer setup and desired flakes are found using the microscope. Since the glass melting temperature of PPC is lower than PC the stacking process used is of multiple release. Each desired flake is brought into contact with the chip(after alignment) with electrodes and the PPC is made to release by raising the temperature to 90°C. The chip is washed with chloroform after each release. While some materials give better thin-flake yield when exfoliating on PPC the multiple release method introduces more contamination between layer which can be and mostly is detrimental to device performance especially for microscopy.

Chapter 3

1T-TaS_2 : A Charge Density Wave Material

This chapter will review previous work reported in literature on 1T-TaS_2. The main aim will be to establish the highly correlated electron nature of the CDW phases which are of interest both from a physics and a device engineering point of view. The crystal structure of 1T-TaS_2 was first studied in 1970's [72] [51] using a transmission electron microscope (TEM). Inside the TEM parallel beam of high-energy electrons are diffracted off the crystal lattice, due to the periodic nature of the crystal the diffracted electrons come together to form a diffraction spot at a plane bellow the sample. A image of this plane has series of spots which correspond to the symmetry of crystal structure. In 1T-TaS_2 it reveals structural phases in the material at various temperatures which are discussed in the first section of this chapter. These phases have been mentioned in the previous chapters and are namely Commensurate(C), Nearly-commensurate(NC) and In-commensurate(IC) CDW phases. The structural transition between these phases greatly affect the transport of electrons in the material, which is evidenced in the in-plane resistivity data presented in the next section. The TEM data motivated questions regarding the ordering of the CDW at the mesoscopic length scale in the room-temperature NC phase. Scanning Tunneling

Microscopy (STM) measurements done in the 1990's [73] [59][74] established that the NC phase has a well-ordered amplitude- and phase- modulated domain structure. These results are presented in the third section. Further investigation of the changes in the band structure across the NC-C transition using Angle resolved photo-emission spectroscopy (ARPES) are presented in section 4. The evidence from the analysis of the reviewed works suggest that electron-phonon and/or electron-electron coupling play an important role in the CDW transitions. Also, in addition to the in-plane CDW inter-layer stacking also plays a part in these transitions. This is most clearly evidenced by structural and electron transport studies done on samples of thickness nearing the atomic limit. These results are presented in section 5. Additionally it has been shown that the highly correlated electron phases of 1T-TaS_2 can be controlled electrically by an applied electric field on the ultra-thin flakes. Electronic control of 1T-TaS_2 has also been attempted using ultra-fast lasers on bulk samples. Both of these are discussed in section 6. We conclude this chapter by the motivation that spatial mapping of the NC-C phase transition in the ultra-thin flakes driven thermally and electrically would help to understand the spatial evolution of the phase transition and resolve questions relevant to device miniaturization.

3.1 1T-TaS_2 Crystal Structure

TaS_2 is a transition metal dichalcogenide which is formed by S-Ta-S layer sandwich layer held together by weak Van der Waals forces. The S-Ta-S layer can have two possible coordination of the metal atoms: octahedral(ABC packing) or trigonal prismatic(ABA packing). They can be further stacked in various ways to get either the pure octahedral 1T, the pure trigonal prismatic 2H, 3R or mixed 2Hb, 6R polytypes. Out of these 1T and 2H-TaS_2 are the most widely studied. Also to note is that both the materials show CDW phases [72] bellow the CDW onset temperature. The 2H phase is more stable at room temperature while the 1T phase is stable at high temperature. Thus fabrication of 1T crystals involves quenching the crystals from above 800°C in a chalcogen environment.

The crystals retain this phase unless heated above 250°C.

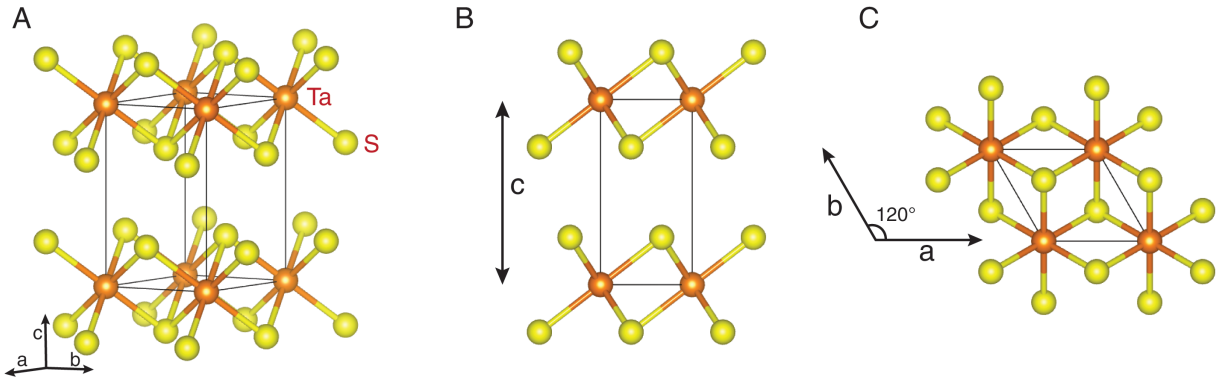

Figure 3.1: Crystal structure of un-distorted 1T-TaS_2. (A) A 3D side view showing 2 covalently bonded 1T-TaS_2 layers which are held together by Van der Waals forces. (B) Side-view of the 3-D structure, looking down from the a-lattice vector. The intra-layer separation is marked by the lattice vector c = 0.5883 nm[49]. (C) Top-view of the 3D structure, looking down from the c-lattice vector. Lattice vector a and b can be identified, they are separated by an angle of 120°. The magnitude of their displacement is same |a| = |b| = 0.3365nm[49]. Figure made using software [38], basic structure crystal structure from [17].

Fig. 3.1 shows the schematic of the real space arrangement of 1T-TaS_2 crystal structure. The figure on the right shows 2 S-Ta-S layers where both layers are held together by weak van der waals type force while each Ta atoms (orange) are covalently bonded with six S atoms (yellow). Each S atom is in turn are bonded with 3 Ta atoms thus fulfilling the stoichiometry of TaS_2. The middle figure shows the lattice looking down from the a-lattice vector. It clearly shows the c-lattice vector that determines the intra-layer spacing which is 0.5883 nm in 1T-TaS_2. The figure on the left shows the lattice looking down the c axis. The vectors defining the displacement between adjacent Ta atoms are the fundamental lattice vectors a and b respectively. The magnitude of their displacement is the same(=

0.3365nm) while they are separated by an angle of 120°. This crystal lattice is measured using TEM in which diffraction images show the reciprocal space lattice vectors (Fig. 3.2). The PLD due to the CDW creates additional satellite peaks which reveal the symmetries of the CDW phases.

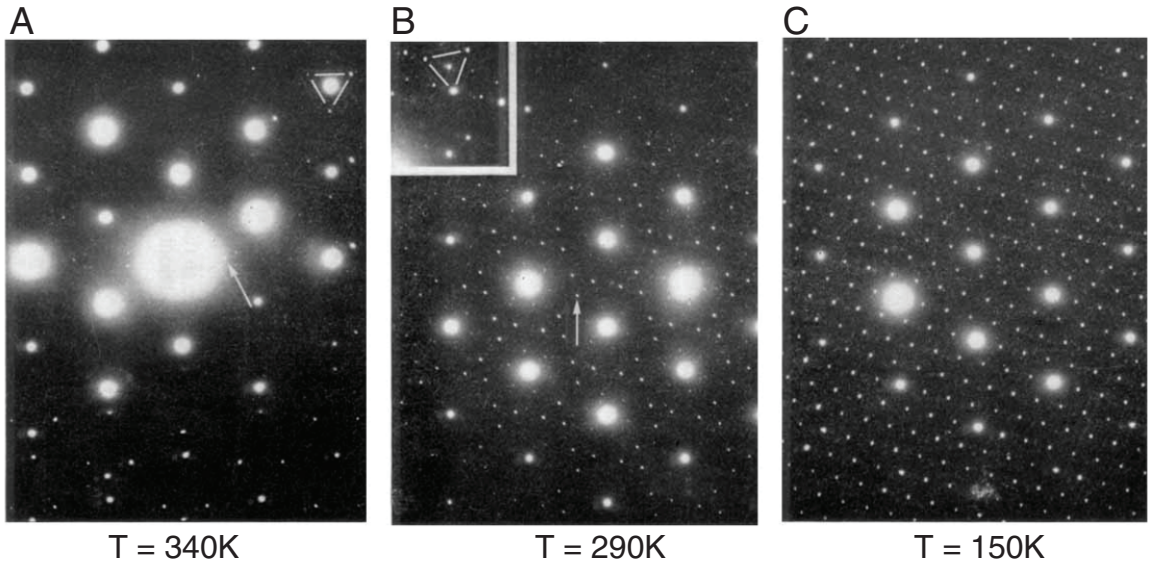

Figure 3.2: Selected area diffraction images of 1T-TaS_2 taken with e-beam parallel to the c* axis. (A) Image taken at 340K shows 1T-TaS_2 in IC phase which shows very weak CDW satellite peaks. (B) At 290 K the NC phase shows much stronger satellite peaks with semi-regular periodicity.(C) At 150 K both the lattice and the super-lattice have uniform intensity and ordering as the material is now in the C-CDW phase. Figure taken from [51]

The diffraction image of 1T-TaS_2 taken at 340K (Fig. 3.2 (A)), show the reciprocal image of the schematic shown in Fig. 3.1(C). The triangularly arranged bright peaks correspond to the original un-distorted lattice. The material is in the IC phase so the PLD superstructure is completely incommensurate with the underlying lattice. Thus, the extra satellite peaks produced by it are very dim in comparison to the un-distorted

lattice. As the temperature is lowered to 290K there is a large qualitative change in the diffraction pattern. The satellite peaks become more visible with respect to the lattice peaks. For comparison the arrow in Fig. 3.2 (A) and (B) points at peaks generating from the same set of scattering vectors. Since the material is in the NC phase the ordering of the satellite peaks is not completely regular. Additional spots grouped triangularly are seen surrounding each spot from the un-distorted lattice. These spots show more additional spots if the electron-beam is tilted slightly. This shown in the inset of Fig. 3.2 (B). Cooling down further to 150K reveals a highly ordered diffraction pattern. Tilting the electron beam does not produce any significant alteration of the pattern. The PLD superstructure is now completely commensurate with the lattice, 1T-TaS_2 is now in the C-CDW phase. While this description is highly qualitative for a mathematically detailed analysis please refer to [51][72]. We will now present the main results of such an analysis.

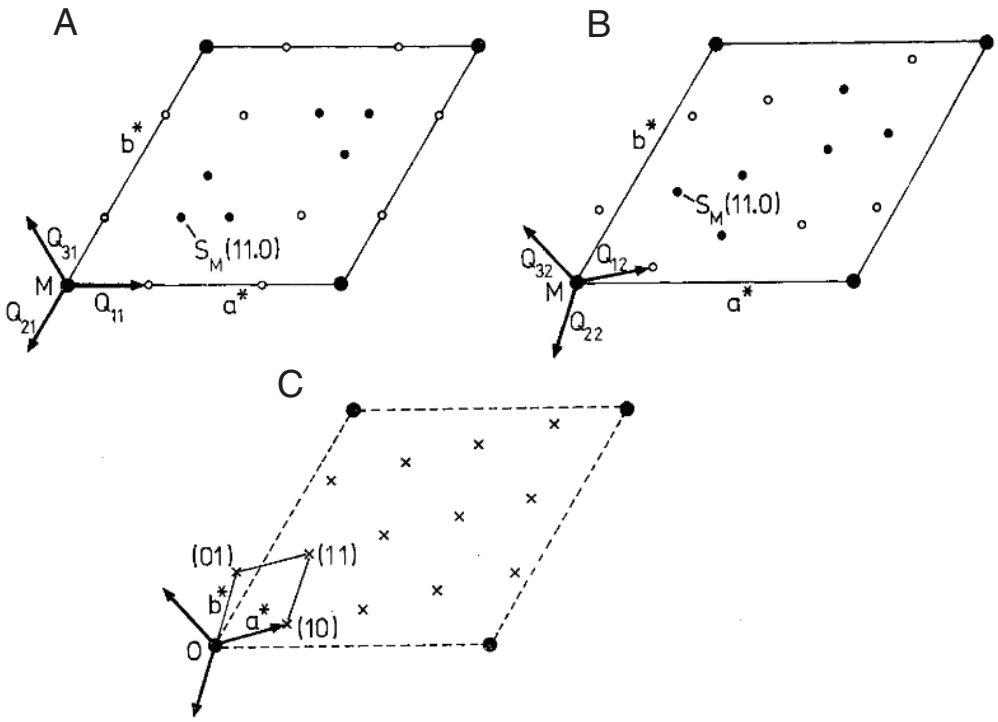

Figure 3.3: Schematic detailing the changes observed in Fig. 3.2. Three symmetric vectors describe the PLD distortion for each phase. (A) The distortion wave-vectors are parallel to the lattice vectors since the ratio of their displacement is not an integer the CDW is in-commensurate. (B) The distortion vectors rotate with respect to the lattice. (C) The wave-vectors now describe a 13.9 ° rotated $\sqrt{13}$ a $\times$ $\sqrt{13}$ a superstructure which is commensurate with the lattice vectors. Figure taken from [51]

Since the satellite spots are trigonally present around spots due to the un-distorted lattice spots, three symmetry-related distortion wave-vectors are used to model the PLD superstructure. This is graphically presented in Fig. 3.3 with reciprocal distortion vectors labeled as Q_{1i},Q_{2i} and Q_{3i}.(i = 1,2,3 for I,NC and C phase respectively). The symmetry of these vectors imply that $Q_{1i}+Q_{2i}+Q_{3i} = 0$ which is known as the triple q condition. Fig. 3.3 shows the spots marked by a triangle in Fig. 3.2 as empty dots and spots pointed by

the arrow as filled dots. In the IC phase Fig. 3.3 (A) the distortion vectors are parallel with the lattice vectors. The PLD is in-commensurate with the ratio of Q/a* being 0.283. For the NC phase the Fig. 3.3 (B) the distortion vectors rotate away from a*. This rotation is temperature dependent, being 11.6° at 331K and increasing to 13.1° at 250K. The magnitude of the Q/a* decreases in the same temperature range goes from 0.286 to 0.282. In the C phase the distortion vectors lock-in with the lattice vectors at an angle of 13.9°. The ratio Q/a* becomes 0.277 which is equal to $1/\sqrt{13}$. In this phase the the distortion can be expressed in terms of the lattice vectors as, $Q_{i3} = 3/13$ a* + 1/13b* or $Q_{i3}' = -3/13$a* + 4/13b*. The C phase gives rise to star-of-david structure which is drawn in Fig. 3.5 (left). It is formed by a group of 13 Ta atoms in which 12 atoms move closer to the central atom. The atomic displacement is around 0.24 Å and is largely in-plane. The displacement of the S atoms is two orders smaller [51] and mostly out-of-plane. There is also an established out-of-plane periodicity in the IC and the NC phase of 3 Ta layers. A possible periodicity of 13 in a two-layer stacking arrangement has been discussed for the C-phase.[56]

While the IC and the C phase have a certain explanation, the nature of the NC state at the mesoscopic scale remained an open question [74] from TEM studies. Theoretical work by Nakanishi and Shiba [39] predicted that the NC phase is not a uniformly incommensurate CDW but has a well ordered amplitude and phase - modulated domain structure. This was later measured and confirmed by STM measurements presented in the next section.

3.2 STM measurements of the NC phase

TEM data for the NC phase of 1T-TaS_2 suggests an incommensurate CDW superstructure. Two separate models were suggested to account for this phenomena. A uniform amplitude and phase rotated ∼12° relative to the atomic lattice which is inferred form a simple extrapolation of the TEM data. The other model was proposed by Nakanishi and Shiba where the CDW's define a hexagonal domain-like structure with a periodicity of 67 Å.

[39] Within the domains the CDWs are commensurate and in-between domains the CDW amplitude decreases and the CDW phase changes. [73] [59] STM imaging shown in Fig. 3.4 established that the latter model was the correct explanation.

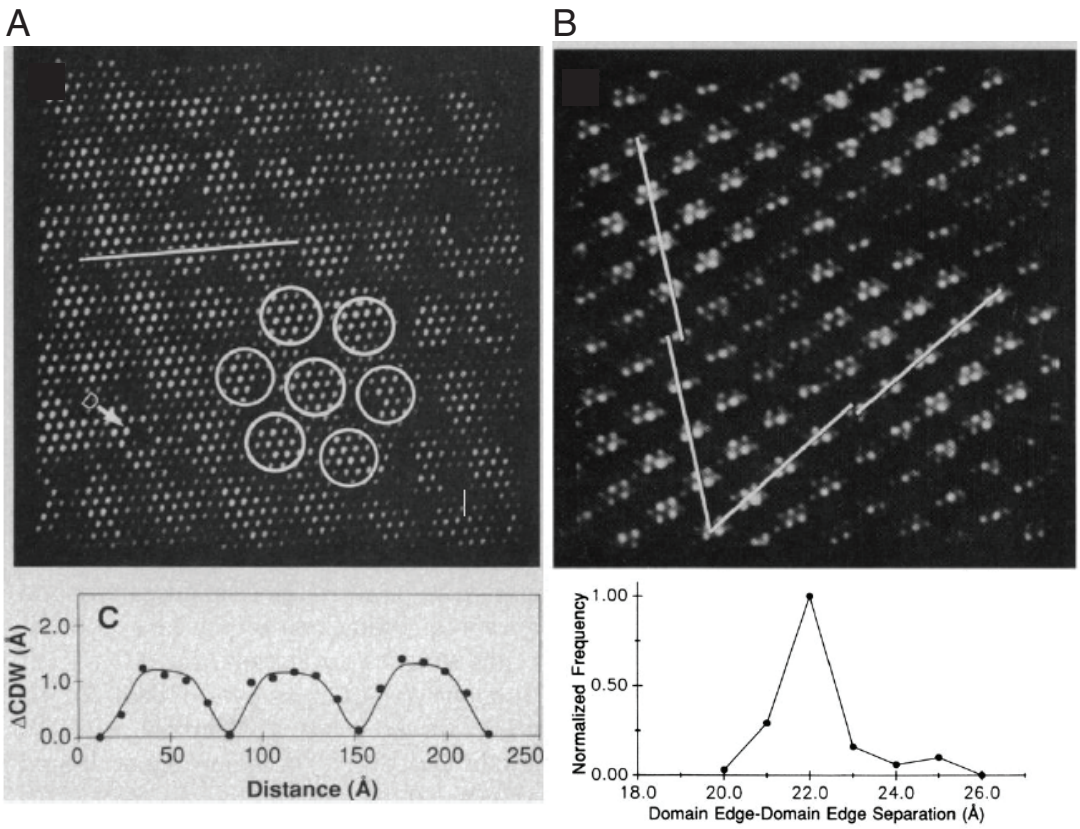

Figure 3.4: STM imaging of room temperature NC phase of 1T-TaS_2. (A) Seven domains of uniform CDW clusters are circled. The line-cut marks the spatial positions for which the data is shown in (C). (B) Atomic resolution data of the domain structure. Lines drawn through adjacent domains show one lattice period phase shift between them. The bottom panel shows the normalized frequencies of experimentally determined distance between CDW maxima at the edges of adjacent domains. Figure (A), (B) and (C) taken from [74], figure (D) taken from [73]

Each dot in the Fig. 3.4 (A) corresponds to a star-of-david, which is roughly 1nm in size. Room temperature STM scans of 1T-TaS_2 show a periodic oscillation in the CDW amplitude (Fig. 3.4 (C)), showing the data from the line cut in panel (A)) with a spatial period of ∼7nm. This modulation defines domains consisting of relatively high-amplitude CDW's separated by regions of lower amplitudes or domain walls.(also referred to as discommensuration or DC lines) Seven such domains are identified in Fig. 3.4 (A) with white circles. Inside the domain the CDW is in the C-phase which is determined by measuring the CDW-lattice angle inside the domains. For the temperature range between 240-340K this value is a constant 13.9°. [73]. Averaging across various domains reproduces the angle seen in the TEM measurements. This confirms the domain model presented by Nakanishi and Shiba. The domain period grows ∼ linearly over the same temperature range from 60-90Å. This growth(melting) of the these hexagonal domains upon cooling(warming) of the NC phase of 1T-TaS_2 at the larger mesoscopic scale are of interest when the NC phase is thermally slowed down and electrically driven in ultrathin-flakes. The hexagonal-domain is itself rotated ∼ 6° relative to the CDW superlattice in a single domain. This rotation implies that a phase shift occurs between the CDWs in adjacent domains. Fig. 3.4 (B) shows an atomically resolved images of the domain structure containing four domains. There are one-lattice period phase shifts between each adjacent domains and can be seen by the displacement between lines drawn across each individual domain. A more rigorous analysis of the arrangement of adjacent domains classifies various possible cases but for simplicity the bottom panel shows the statistical frequencies(normalized) of measured distances between the CDW maxima of adjacent domains. The average distance is ∼ 20Å which accounts well with the one-lattice period phase shift model. A single lattice period shift thus marks the beginning of a DC line. In order to satisfy the triple q symmetry condition of distortion vectors this can only happen in triplets. This also applies when the period shift reveres itself and the DC line is annihilated. Thus the nucleation and annihilation of DC lines connecting a dislocation - antidislocation pair can happen only in triplets. This explains the Kagome like hexagonal tiling of the C-CDW like domains in the NC phase.

While structural details reveal important information regarding the spatial information

of the CDW, electron transport in the material is of importance from a device application perspective. Electron transport in 1T-TaS_2 is affected quite strongly by the CDW/PLD distortion. This is explored using resistivity and ARPES measurements in the next two sections.

3.3 Electron transport in 1T-TaS_2

The onset and transitions of the CDW superstructure heavily affects the electron transport behavior in 1T-TaS_2. Each structural transition is accompanied by a metal-insulator transition.

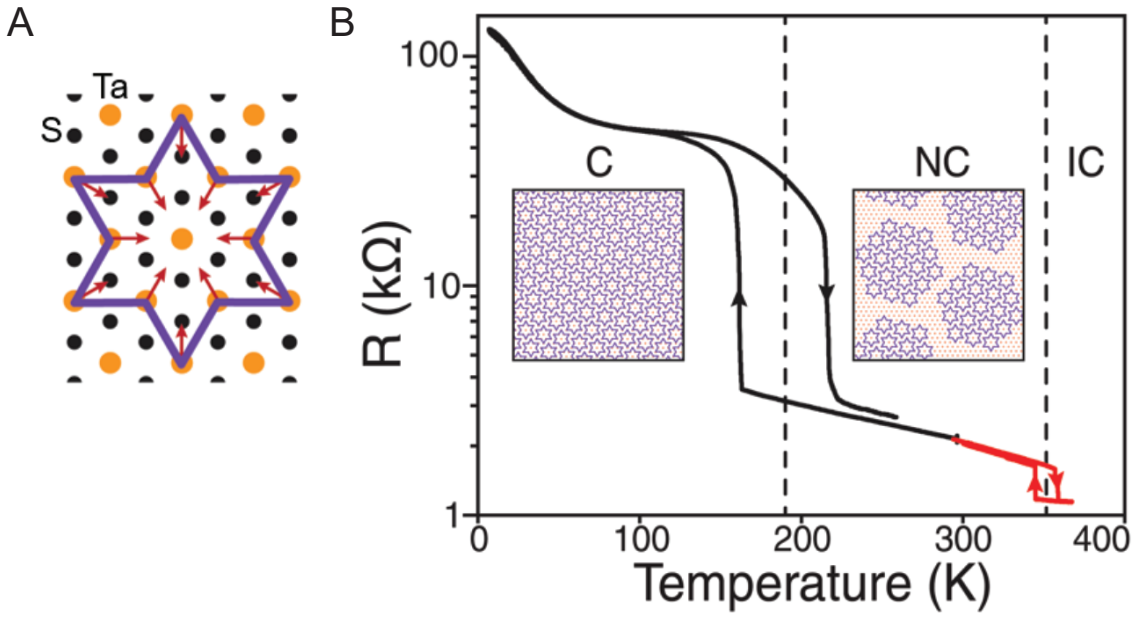

Figure 3.5: In-plane resistance of 1T-TaS_2 showing the CDW transitions. (A) The C-CDW takes a $\sqrt{13}a \times \sqrt{13}a$ superstructure that forms Star-of-David like clusters with the outer 12 atoms moving slightly inward towards a central atom. (B) Cooling down from about 550K the material is in metal-like IC phase with low resistivity. At $\sim$ 350K the a first-order transition marks the onset of the NC phase which is more resistive(red line). Cooling down further there is a stronger metal to insulator transition from NC to the C phase at 180K which reverses itself at around 220K upon warming(black line). The resistance of C phase below $\sim$100K shows behavior of an insulator. Insets show a schematic distribution of the star-of-david's in C and NC phase.

Fig. 3.5 shows the resistance data taken on a $\sim$ 20 nm thick 1T-TaS_2 flake contacted in a lateral electrode geometry. The in-plane resistance values show the onset of the various CDW phases as a function of temperature. The resistivity behavior above 350K in the IC-CDW phase is more metal like. As the temprature is lowered (Fig. 3.5 red line) a sharp metal-to-insulator transition marks the onset of the NC-CDW phase. Cooling the material

further (Fig. 3.5 black line), the temperature dependence of the resistance of the NC phase is more semi-metallic. At 180K the material transitions to the C-CDW phase. The resistance jumps by an order of magnitude as reported in resistivity studies elsewhere [72] [26]. Below the transition temperature the resistance roughly flattens until ∼100K after which it shows an insulator like behavior. Upon warming the transitions reverse themselves but with a hysteresis which reveals the metastability of each phase. The C-CDW phase transitions to NC-CDW phase at around 220K showing a large hysteresis of ∼ 40K. The NC-phase transitions to the IC phase with a much smaller hysteresis of only a few kelvin around 350K.

Hall measurements [26] reveal the nature of the electrons at the Fermi surface. A negative hall-coefficient (R_H) at 360K indicates electron like carries in the IC-CDW phase with a carrier concentration of $\sim 10^{22}$ cm^{-3}. A sharp discontinuity marks the NC-IC CDW transition and the hall-coefficient increases gradually that shows that the carrier concentration decreases in the NC phase. From 350K to 200K it is reduced by roughly an order of magnitude. The NC to C transition at 180K brings a change in the polarity of R_H and a reduction of charge carriers from $\sim 10^{21}$ cm^{-3} to $\sim 10^{19} cm^{-3}$. The temperature dependent hysteresis appears the same as the resistance data. R_H increases steeply in the C phase upon further cooldown having a maxima at 30-50K and a minimum around 4K. This behavior is similar to that of an extrinsic semiconductor showing impurity conduction. Low temperature electron transport has been explained using Anderson localization [13] where the conduction is extremely sensitive to disorder.

The transport data thus suggests that the IC phase has a metal-like fermi surface and has electron like carriers. At the transtion into the NC phase the carrier concentration decreases but remains fairly constant upon cooling indicating that the phase is still metal-like. At 180K when the material transitions into the C phase the charge carrier concentration decreases significantly and the sign of the carriers reverses. Temperature dependence in the C-CDW phase additionally show that the material is now a semi-metal or a semiconductor. This indicates that a large portion of the fermi-surface has been destroyed. This change in the fermi surface is measured using ARPES whose results are shown in the

next section.

3.4 ARPES : Band Structure visualization

Structural transitions observed using TEM and first-order phase transitions observed in the in-plane transport data suggest that the transition from the IC to the C CDW phase is accompanied by a significant restructuring of the band diagram. It has been estimated that the formation of a perfect $\sqrt{13}a \times \sqrt{13}a$ in a closely related material, 1T-$TaSe_2$ destroys at-least 90% of the fermi surface. These changes can be visualized using angle resolved photo-current emission spectroscopy or ARPES.

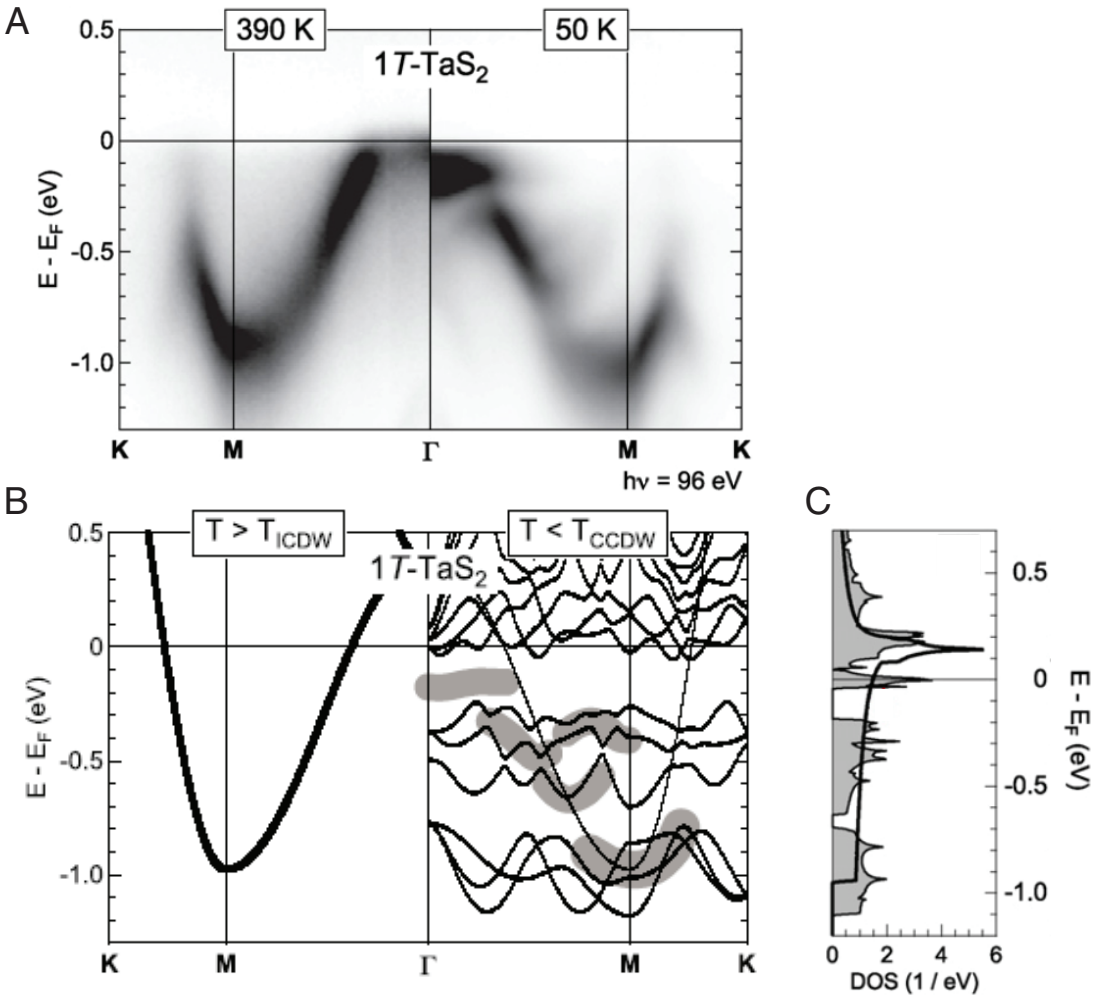

Figure 3.6: ARPES measurements of 1T-TaS_2 visualize changes in the bandstructure close to the fermi-surface. (A)ARPES intensity maps taken at 390K and 50K show the fermi-surface and the underlying bands in IC and C - CDW phase respectively.(B) Band-structure calculations of 1T-TaS_2. A regular tight-binding model is shown for the IC phase(left), a re-constructed bandstructure using the $\sqrt{13} \times \sqrt{13}$ modulation. Features that carry significant spectral weight in the C-CDW phase are highlighted in thick gray line.(C) Density of states(DOS) of the unreconstructed(solid black line) and reconstructed(filled gray curve) bandstructure. Figure taken from [49]

Fig 3.6 (B) shows a tight-binding calculation for 1T-TaS_2. A single Ta 5d band disperses downward from the Brillouin zone center (Γ point) toward the M point (zone boundary) and then back upwards along the M-K direction (zone face). It thus crosses the Fermi-surface twice and to give an elliptical Fermi surface pocketed around the M point. This band is visible in the ARPES data taken in the IC-CDW phase at 390K shown in Fig 3.6 (A) (left). In the C-CDW state the band is re-arranged and the 5d band is split into sub-manifolds shown in Fig 3.6 (B) (right). Features along the original band carry most of the spectral weight as shown by the thick gray lines. Thus the features of the reconstructed band are only faintly visible in the ARPES data taken at 50K (Fig 3.6 (A) right) in the C-CDW phase. The onset of the C-phase rearranges the Ta 5d band in a Mott-Hubbard type metal-insulator transition where the charge is localized at the center of the star-of-david pattern. The Hubbard subband overlap creating a pseudo-gap ($\sim$0.4eV) at the Fermi surface (E_F) [49]. This leads to the appearance of a sub-band around the Γ point at $\sim$0.2eV bellow E_F in the ARPES data. Thus strong electron-phonon coupling and electron-electron correlations are present simultaneously in 1T-TaS_2. While the reconstruction model presented explains the qualitative features of the sub-manifolds, for features closer to the Fermi surface further analysis and understanding of the bandstructure would require to include both the PLD reconstruction and spin-orbit interactions [25]. In a recent experiment combination of ARPES and X-Ray Diffraction (XRD) results have shown the existence of bi-layer stacking [71] in the C-CDW phase. This would make the low-temperature state of 1T-TaS_2 a band insulator with two electrons fully occupied [30] [48] in the flat band near E_F in the ARPES data. Consequently STM spectroscopy done on the bulk sample to investigate the DOS at an atomically sharp cleavage plane [8] [9]. Considering most of the bulk state to have dimerized, the cleavage point is a breakdown of the bi-layer condition where the DOS states should be metallic. But a spectral gap (smaller than paired layers) observed in the unpaired layer can still be attributed to Mott localization.

This section ends the review of the work done on the bulk 1T-TaS_2 crystal. Recent research has focused on studying the crystal in the ultra-thin limit and achieving control of the correlated electron state. Which will be the focus of the next two sections.

3.5 Ultra-thin 1T-TaS_2

Recent increase in the interest of the study of two-dimensional materials in the atomic limit has focused on exploring new physics and novel electronic properties in reduced dimensions. [20] [42] [28]. Due to it's multiple CDW transitions 1T-TaS_2 has become the focus of study for the effect of such thinning on the stability of it's correlated electron phases and possible application as a memristive material.[64][76][24]. Initial studies on flakes exfoliated in ambient conditions reported the absence of the NC-C CDW transitions in flakes bellow a certain critical thickness.

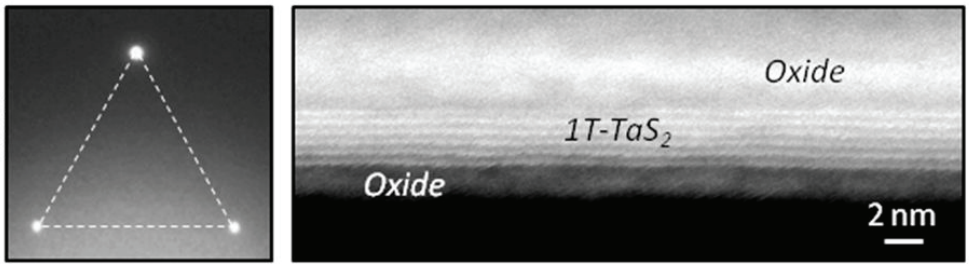

Figure 3.7: Flakes exfoliated in ambient atmosphere develop an amorphous oxide layer, visible in a cross section electron microscopy image(right). A TEM image of such flake shows absence of CDW order.(left) Figure taken from [64]

This was later attested to the surface oxidation of the flakes. A cross section electron microscopy image shows this amorphous oxide. Fig 3.7(right) Such oxidation causes sufficiently strong surface pinning that destroys charge ordering in these flakes which is evident by the absence of any satellite peaks in the TEM diffraction images (Fig. 3.7(right)) of such flakes.

To prevent such oxidation the exfoliation of 1T-TaS_2 is carried out in a N_2 filled glove box with O_2 and H_2O levels beneath 1-ppm. Additionally these flakes or devices made with them are capped with a protective h-BN layer before exposure to ambient environment

outside the glove-box.[64] Such capping has been utilized to stabilize a variety of 2-D materials which are sensitive to oxidation since h-BN is a very well known and highly stable 2-D material with a large band-gap (5.2eV).

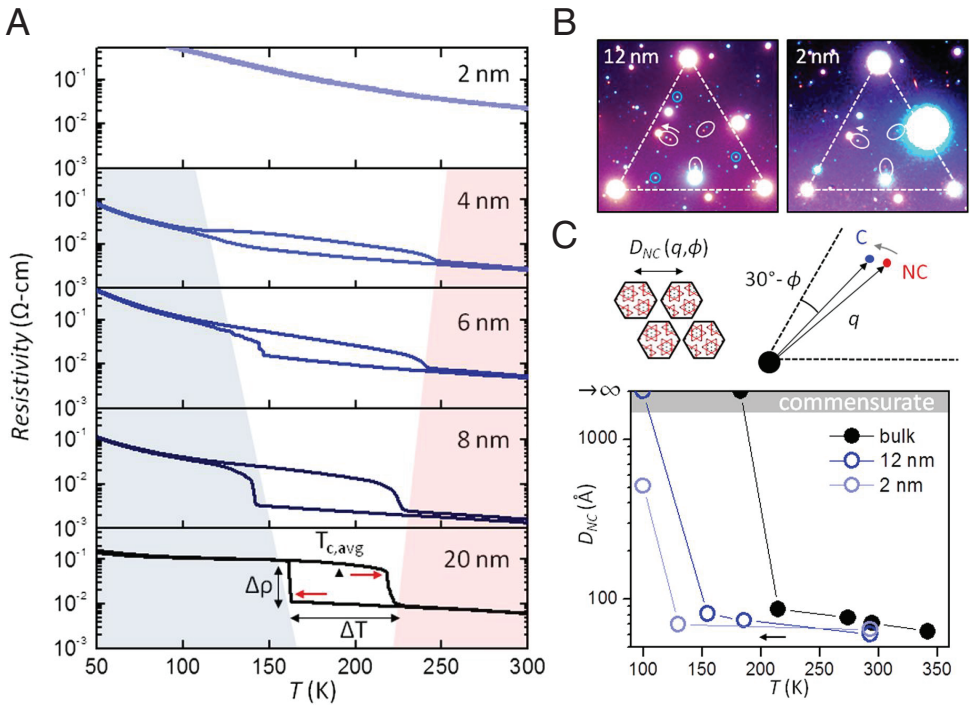

Figure 3.8: Protected ultra-thin 1T-TaS_2 flakes show NC-C CDW phase transitions.(A) Protected thin flakes with thickness down to 4nm show the NC-C thermal hysteresis in the R vs T data. Widening of the hysteresis upon thinning is shaded. (B) TEM data of h-BN capped 1T-TaS_2 flakes of 12nm and 2nm thickness, taken at 295K(red peaks) and 100K (blue peaks). (C) (Top) Position of the satellite peaks can be used determine periodicity of the commensurate domains in the NC phase D_{NC}. (Bottom) The NC to C transition temperature is lowered with reduced thickness. Figure taken from [64]

For such protected devices the NC-C transition is seen in the in-plane transport data for flake thickness down to the 4nm limit. Fig 3.8(A) With decreasing flake thickness the

thermal hysteresis NC-C phase transition becomes wider. While the center of the hysteresis does not change substantially the difference between the transition temperature to the NC and C phase increases from $\sim$ 50K to $\sim$110K. This indicates that the thinning does not stabilize either the NC or the C phase but increases the energy barrier separating the NC and C phases. Thus, in thin samples the meta-stability of the NC(C) phases is increased upon cooling(warming). This is corroborated with TEM data taken on these samples. Fig 3.8(B) shows TEM diffraction images taken for a 12nm and 2 nm h-BN protected 1T-TaS_2 flakes at 295K(red dots) and 100K(blue dots). While the protective h-BN introduces additional diffraction spots it is still possible to identify the satellite peaks of the CDW structure which is demarcated by white ellipses. The movement of the satellite peaks can be related quantitatively to the to the periodicity of the the commensurate domains D_{NC}, in the NC-phase.[59] A qualitative schematic is shown in Fig 3.8(C) (top). As seen in the STM data [59][73] the room temperature D_{NC} is $\sim$7 nm which is similar to what is seen for both the thin flakes.Fig 3.8(C) (bottom) As the sample is cooled the domain size for the 12 nm flake grows to $\sim$ 8-9 nm after which it jumps to an arbitrarily large value indicating the onset of the C-CDW phase. For the 2-nm flake on the other hand the flake remains in the NC phase down to 100K but the domain size increases to 50nm indicating that the phase transition has started to happen.

This has been explained by the increased cost of energy to remove DC's from the NC phase in the 2-D limit. [64] In bulk samples the intra-layer stacking of the NC domains make the DC's planar objects which are difficult to pin by point like impurities. In the 2-D limit they become line-like and thus more susceptible to be pinned. This would slow down the growth and annihilation of DC's which would appear as increased meta-stability of the phase transitions.

These results partially motivate the study in this thesis. The sharp first-order NC-C phase transition in the resistitvity of bulk 1T-TaS_2 becomes more multi-step in ultra-thin flakes (6nm flake resistance data around 150K on cooling Fig 3.8(A)) That combined with the TEM results indicate the slowing down of the NC-C phase transition. Mapping the distribution of the NC and C domains at a mesoscopic scale in these intermediate resistance

states is the aim of our device geometry.

3.6 Electrically controlled Phase Transitions in 1T-TaS_2

Various methods have been shown to induce changes in the electronic structure of 1T-TaS_2. Superconductivity can be induced by applied pressure [53] and intercalation by Fe [31] or Se [34] ions. Electrical pulses applied at the at the atomic scale using a STM tip shows formation of a 'Metal Mosaic' [35] [12] like discommensuration structure in the C-phase at 6.5 K. Additionally, electrical pulses above a certain threshold and time scale have been shown to drive the metal-insulator transition [67] at low temperatures.

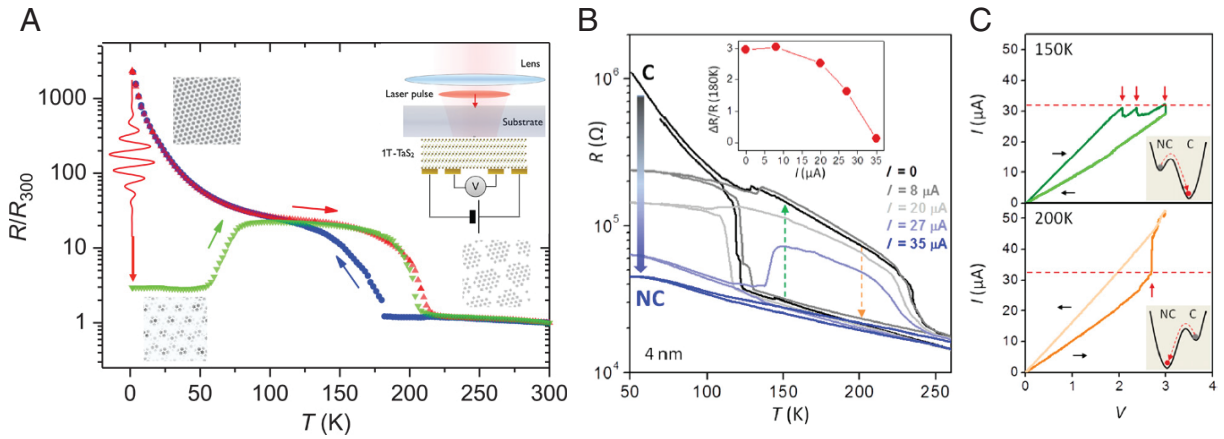

Figure 3.9: Electrical control and manipulation of the CDW phase in 1T-TaS_2. (A) Ultra-fast optical pulse induces a metallic state in C-CDW phase of 1T-TaS_2.(B) In-plane current can suppress the NC to C transition in thin flakes. (C) Ultra-thin flakes electrically driven into intermediate states between the NC and C-CDW phase at a temperature where the current state is meta-stable. Figure (A) taken from [66], Figure (B), (C) taken from [64]

Fig 3.9 (A) shows the temperature dependent resistance of a 1T-TaS_2 flake with 20nm-100nm thickness. The red and blue curve show the typical behavior for the crystal. At low temperature a single 35-fs optical pulse above a threshold fluence drives the insulating C-CDW into a highly conductive state with a drop in resistance of around 3 orders of magnitude. The C phase is later recovered upon warming above 50K. Ultra-fast lasers have also been used previously to melt and image the recovery of the CDW order in the time scale of ∼pico-seconds [16]. This motivates that understanding the physics and the realizing control of this strongly correlated system could enable novel device applications.

Ultra-thin samples have also motivated the control of these CDW states. Multi state metal to insulator switching has been shown in flakes of thickness between 10-20nm.[76][24][75] Fig 3.9 (B) shows the hysteresis curve for a h-BN capped 4nm thick 1T-TaS_2 flake with negligible current flow(black curve), which is very typical for the material. When the material is cooled while flowing increasingly large in-plane current the NC-C phase transition is suppressed [64]. Even when the current is switched off at low temperature the NC state is maintained. This shows that in ultra-thin flakes it is possible to maintain the NC phase at temperatures where it is not thermodynamically stable. Additionally if the flake is in the NC phase at 150K it is possible to drive it into the C-phase by an applied electric field Fig. 3.9 (C)(Top). The material initially shows typical ohmic behavior until a certain current value after which the I-V behavior is non-linear as the current drops with increasing voltage. Sweeping the voltage back to zero does not reverse this process as the resistance is now larger than at the beginning. The reverse of this process can also be done by starting with the material in the C phase at 200K (Fig. 3.9 (C), bottom).

The possibility of such driving in the ultra-thin flakes is the second motivation for our spatial mapping of the NC-C transitions in these flakes. The distribution of the NC and C domains in the intermediate states of electrical driving in comparison with thermally driven intermediate states should give an insight regarding the spatial dynamics involved in these transitions.

Chapter 4

1T-TaS_2 : Photocurrent Microscopy

Previous works on ultra-thin flakes of 1T-TaS_2 motivate the study of spatial evolution of the NC-C phases transition in such systems. In the following chapter we propose a device geometry that would enable such a study. In the first section we discuss the working of this geometry and present the proof of principle regarding the same. In the next section we present the spatial evolution of the NC-C CDW phase transition upon thermal cycling as evidenced by zero-bias photocurrent microscopy. After that we show the data for the electrically driven NC-C CDW transition and the concomitant photocurrent maps in section 3. Section 4 presents a phenomenological model for the multi-step NC to C electrically driven transition based on past theoretical work. In section 5 we discuss the model in relation to the experimental data obtained.

4.1 Vertical heterostructure design for Photocurrent Microscopy

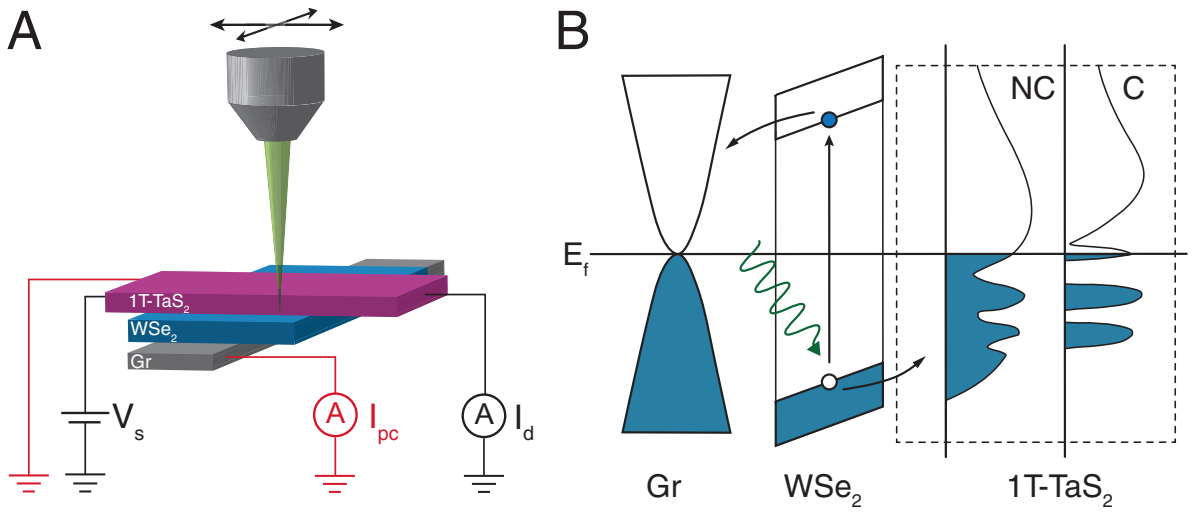

Figure 4.1: Simultaneous electrical driving and photocurrent detection of NC-C CDW transition in 2D 1T-TaS_2. (A) Schematic of device heterostructure and measurement geometry. Lateral contacts to 1T-TaS_2 allow measurement of resistance and electrical driving, whereas vertical contacts give photocurrent at zero bias. (B) Band structure diagram showing mechanism of photocurrent generation. Photo-generated electron-hole pairs in WSe_2 separate due to the intrinsic electric field created by the work function mismatch between 1T-TaS_2 and graphite, which changes across the NC-C transition.

In order to spatially map the NC-C metal-insulator transition at the micron scale we utilize highly efficient photo-current generation in nanometer thin WSe_2. [6] A schematic of our unique device and measurement scheme is shown in Fig 4.1 (A). A scanning, focused laser (520 nm wavelength) impinges on a heterostructure junction consisting of (from top to bottom) 1T-TaS_2 , WSe_2, and graphite (Gr) thin flakes. Photo-generated electron-hole

pairs in WSe_2 separate due to the intrinsic electric field created by the work function mismatch between 1T-TaS_2 (5.2eV) [52] and graphite(4.6eV) [58], which changes across the NC-C transition. Fabricated devices are additionally capped with h-BN to prevent atmospheric degradation of the 1T-TaS_2 flake as shown in previous studies. [64] Large band gap energy of h-BN ensures that it does not effect the photoelectric response of the device.

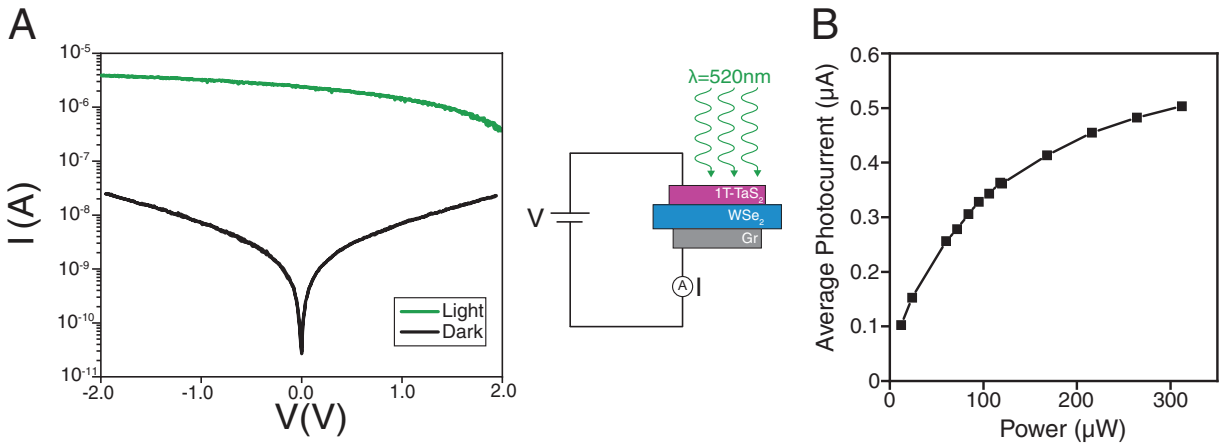

Figure 4.2: Photocurrent response of a typical heterostructure device.(A) I-V characteristics across 1T-TaS_2/WSe_2/Gr junction with and without laser left to it is the schematic of measurement geometry.(B)Zero-bias photocurrent vs. laser power incident on sample.

In the absence of light, the resistance across the WSe_2 junction is relatively large ($\geq$100MΩ). In presence of light, the electron-hole separation yields a local, vertical photocurrent, I_{pc}, even when no bias is applied to the junction. This can be seen in voltage-current characteristics presented in Fig 4.2 (a). The photocurrent I_{pc} changes sub-linearly with incident laser power as shown in 4.2 (b). This is consistent with previous studies in graphene/MoS_2/graphene junctions. [6] Across the NC-C transition, the band structure of 1T-TaS_2 undergoes a reconstruction, which should manifest as a change in I_{pc}. A cartoon representation of such a change is shown in Fig.4.1 (b). Scanning the laser spot across our

sample allows for the C and NC domains (as well as intermediate meta-stable states) to be imaged spatially with diffraction-limited resolution (∼1 μm). The 1T-TaS_2 is additionally contacted with two leads laterally outside the junction area, so that its resistance (∼10 kΩ) can be monitored and the NC-C transition be driven electrically like that in previous works [64] [75] [24]. This geometry is more complex in both fabrication and the origin of photocurrent than the simpler and more common planar, two terminal photocurrent device geometry. [63] [44] [62] We have found them to yield less direct information on CDW domain structure in 1T-TaS_2 [B].

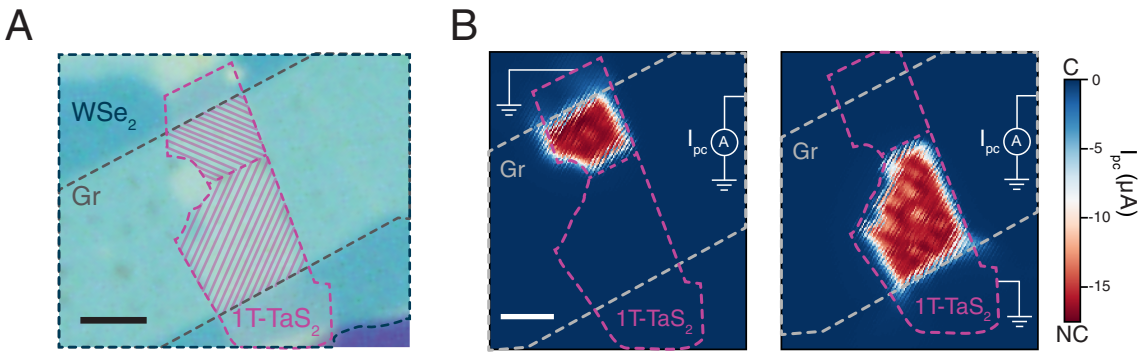

Figure 4.3: (A) Optical image of a device with 5 nm-thick 1T-TaS_2 with flake edges traced out and 1T-TaS_2/ WSe_2/Gr junction shaded for clarity. Scale bar is 5 μm.(B)Photocurrent map of the same sample. The discontinuity in the middle of the flake is not visible under optical or AFM imaging but is evident in photocurrent maps taken with geometries in which only one of the contacting lead is grounded at a time.

Fig.4.3(A) shows an optical image of a device of the proposed geometry. The 1T-TaS_2 thickness is 5nm (see Fig A.1) and has a discontinuity at the narrowest region. This is most evidently seen in photocurrent maps of the device taken with different lead combinations Fig. 4.3(B). While this prevents any lateral electrical driving, it does not impede the measurement of thermal evolution of the transition.

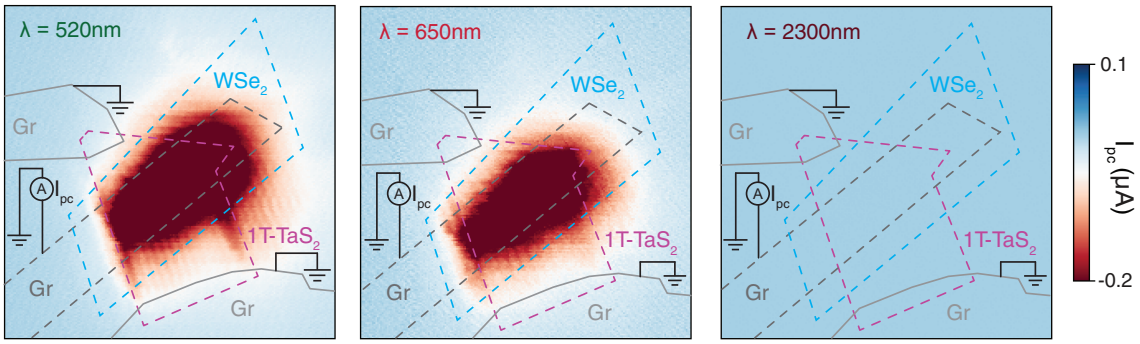

Figure 4.4: Photocurrent map of device with 5-8 nm 1T-TaS_2 flake taken with light of reducing energy(left to right). Plotted on the same scale bar, the photocurrent generated for light with energy bellow the WSe_2 bandgap($\lambda = 2300nm$) is negligible in comparison.

In order to confirm that the photocurrent originates from the process illustrated in Fig.4.1 (b), we took photocurrent maps with lasers of varying energies Fig. 4.4. The direct (indirect) bandgap for bulk WSe_2 is $\sim$1.6eV ($\sim$1.2eV).[77] Clear photocurrent is observed at the 1T-TaS_2/WSe_2/Gr junction for laser of wavelength 520nm(2.38eV) and 650nm(1.91eV) as they have energies much larger than the WSe_2 bandgap. The 2300nm(0.54eV)wavelength laser has energy below the bandgap and thus no photocurrent signal of comparable magnitude is observed. Please note that the first two images (from the left) have been saturated to compare with the third.

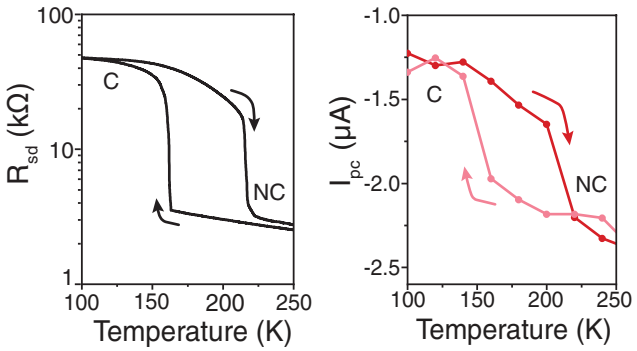

Figure 4.5: Average photocurrent response of device with a 22nm 1T-TaS_2 flake as a function of temperature. The negative sign of I_{pc} agrees with scheme presented in Fig 4.1. The sharp increase and decrease in the magnitude of photocurrent(left) tracks the in-plane resistance measured simultaneously(right) indicating that our proposed geometry should track the NC-C CDW transition.

The last confirmation of our proposed geometry is to monitor the temperature evolution of I_{pc}. In Fig 4.5, we compare the temperature dependent later resistance $R_{sd} = V_s/I_d$ for a device with a moderate 1T-TaS_2 thickness of 22 nm, to that of photocurrent, I_{pc}, with laser defocused across the junction region. Both show the abrupt and hysteretic NC-C transition centered at ∼190 K that is characteristic of bulk like 1T-TaS_2, indicating the validity of our measurement scheme. The negative sign of I_{pc} indicates that photogenerated electrons (holes) flow into Gr (1T-TaS_2), consistent with the work function difference scheme.

4.2 Photocurrent Mapping of thermal NC-C transition

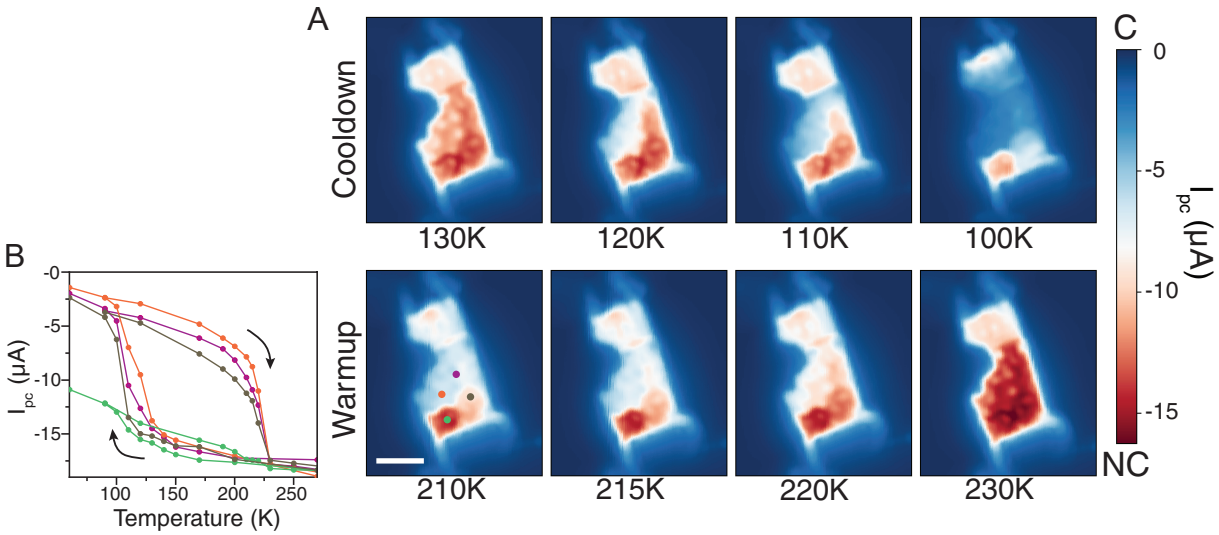

Figure 4.6: Photocurrent imaging of the temperature-induced NC-C transition in the device shown in Fig.4.3 with 1T-TaS_2 flake of 5nm thickness. (A) Photocurrent maps taken at various temperatures across the NC-C transition for cooling and warming show formation of micron-sized domains. Scale bar in the bottom left panel is 5 μm. (B) Temperature-dependent photocurrent signal from four different color-coded locations marked in the bottom-left panel of (A). Each points marks a region with distinct transition temperatures and intermediate meta-stable states.

Photocurrent images of the junction area (with both contacts to 1T-TaS_2 grounded) are shown in Fig 4.6 as a function of temperature for both cooling and warming around the transition temperature. Red (blue) region is where I_{pc} is larger (smaller) in magnitude and corresponds to those more in the NC (C) phase. At higher temperatures, the entire area is relatively uniform and in the NC phase, although there is a marked difference across the discontinuity. The spotlike features are attributed to small bubbles or unwanted particles

at the interface and likely do not reflect true features of the CDW phases. (See Appendix Fig A.2) At lower temperature, different areas of the junction transition into the C phase at different temperatures and to varying degrees, manifesting in formation of micron-sized domains in the photocurrent image. In order to show the regional differences more explicitly, the bottom-left panel shows the plot of temperature-dependent photocurrent values at four different locations marked by the colored points in the bottom left image at 210K. Overall, the hysteresis between cooling and warming is wider than that for the thicker sample shown in Fig. 4.5, which is consistent with previous transport studies.[64] Upon cooling, the temperature at which the transition into the C phase begins varies over 25 K across the four locations, while the abruptness of the transition is also different. In particular, orange and purple traces show several metastable states with intermediate I_{pc} that is absent in the gray trace. In contrast, upon warming, all locations complete the transition into the NC phase at ∼225 K. Interestingly, the location marked in green maintains a relatively large I_{pc} throughout the entire temperature range, indicating that it remains nearly locked in the NC phase, although a small hysteresis loop is still visible. Such an effect has also been seen in transport measurements on ultrathin samples, although no spatial information was obtained.[64]

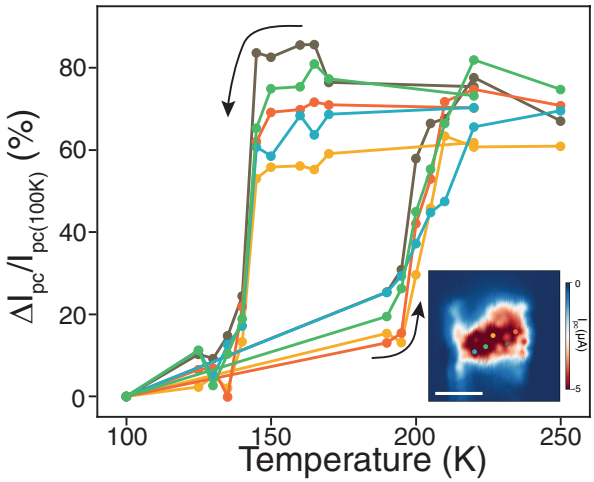

Figure 4.7: Photocurrent evolution over various points in 22nm 1T-TaS_2 flake shows a smaller temperature hysteresis in accordance with the transport data. The spatial uniformity of the transition is evident as all points show the transition at the same temperature. Scale bar is 5 μm (inset)

To compare with the ultra-thin sample Fig 4.7 shows temperature evolution of I_{pc} for a sample with 22 nm-thick 1T-TaS_2 flake, which shows a narrower hysteresis, more abrupt NC-C transition, and more complete transition into the C phase across the entire junction. This is also consistent with previous nanoscale infrared imaging on a 1T-TaS_2 flake with moderate thickness.[18] These measurements demonstrate the utility of our photocurrent scheme in deciphering spatial differences in the NC-C transition of 1T-TaS_2 on the micron scale which are relevant for electronic devices.

4.3 Electrically driven transition

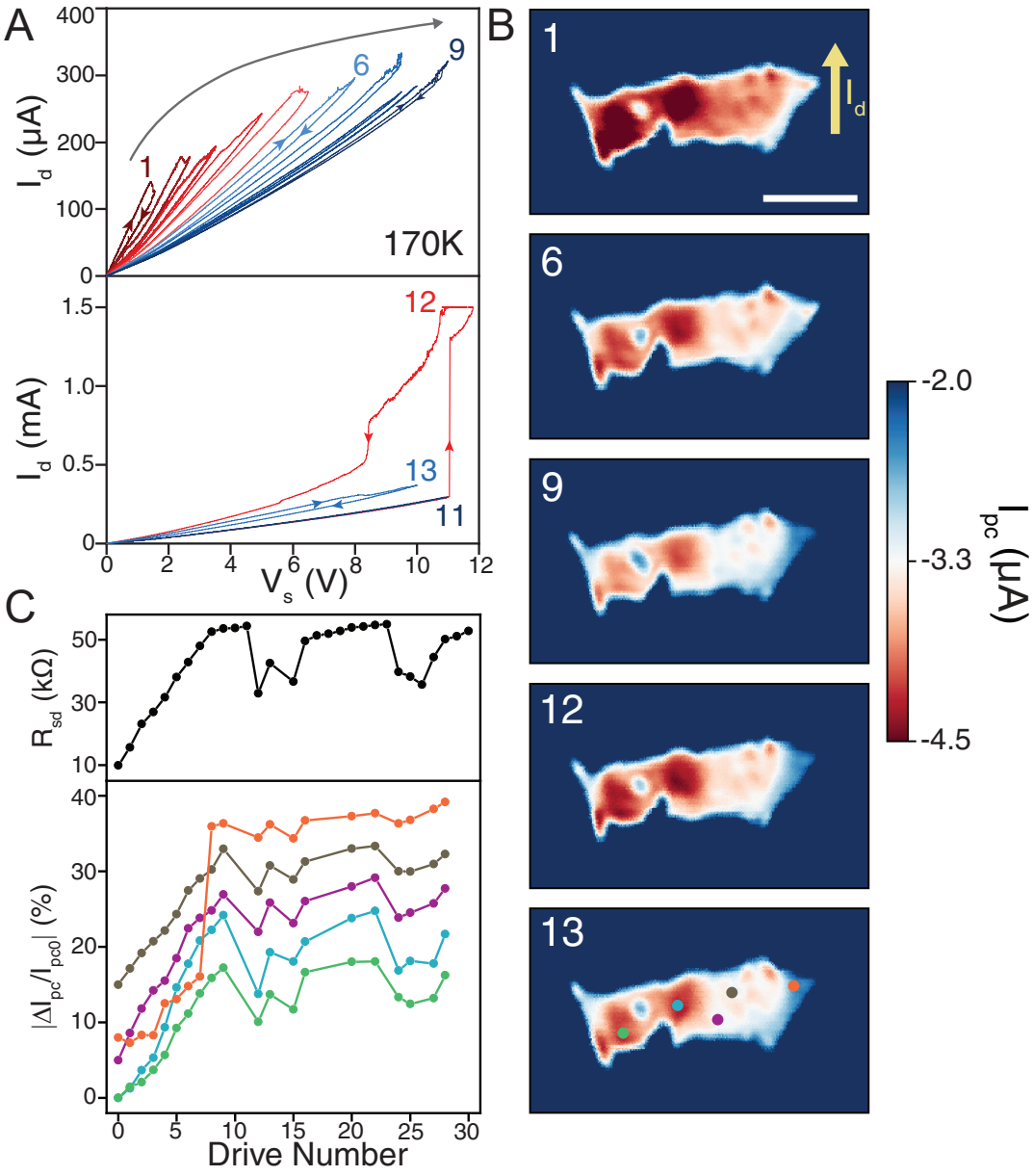

Figure 4.8: (Caption next page.)

Figure 4.8: Reversible electrical driving of metastable states across NC-C transition and concurrent photocurrent imaging. (A) Sequential current-voltage sweeps taken at 170 K starting in the NC phase on a 5-8 nm-thick 1T-TaS_2 device. The top panel shows a gradual decrease in conductance from sweeps 1-9. The bottom panel shows an abrupt increase in conductance in sweep 12 and decrease again for sweep 13. (B) Photocurrent maps taken after selected sweeps show changes following the resistance trend without domain formation. Scale bar is 5 μm. (C) Top: lateral 1T-TaS_2 resistance before each voltage sweep measured at low bias. The multiple resistance states can be switched back and forth repeatedly at a fixed temperature. Bottom: photocurrent change (in percent) for various color-coded locations marked in the bottom image in (B). The traces have been offset for clarity. All locations show photocurrent tracking the overall resistance.

In the upper panel of Fig 4.8(A), shows a series of slow, lateral current-voltage sweeps (0.13 V/s maximum) taken on another device with 1T-TaS_2 thickness of 5-8 nm starting in the NC phase at 170 K. Initially, I_d increases linearly with applied V_s until a sudden decrease is observed at a relatively small voltage value of $\sim$1.4 V, after which we sweep V_s back to zero. As the measurement is repeated, the conductance decreases after each subsequent sweep while the current-voltage characteristics become increasingly nonlinear. This process gradually transitions the 1T-TaS_2 sample further into the C phase with higher resistivity and nonlinear conduction.[65] The voltage needed to drive the current decrease increases with the sweep number, although the I_d-V_s characteristics appear to eventually saturate onto a single curve (see sweep 9). The upper panel of Fig 4.8(C) plots R_{sd} at low bias with sweep number before each sweep, which also begins to show a saturation after sweep 9. Note that this saturated resistance level is 63% of the resistance of the C phase driven by temperature at 170 K, indicating that conducting discommensurations still remain.

In this saturated, metastable state close to the C phase, increasing V_s further to a larger value of $\sim$11 V at the same temperature of 170 K induces an abrupt current rise, as can be seen in sweep 12 in the lower panel of Fig 4.8(a). Upon sweeping Vs back to

zero, the current abruptly decreases at a lower voltage of ∼8.5 V but does not return to its original state. As a result, the device can be switched back toward the NC state with higher conductance in a nonvolatile manner. We have repeated this driving procedure with additional sweeps and the corresponding resistances are shown in the upper panel of Fig 4.8(c), which demonstrates that 2D 1T-TaS_2 can be switched bidirectionally back and forth between the NC and C-like states at a fixed temperature.

Such electrically induced effects could potentially arise from the formation and switching of micron-sized NC or C domains, as in the case of the temperature-driven transition shown in Fig 4.6. To address this issue, we further performed zero-bias photocurrent scans after many of the voltage sweeps, and five selected images are shown in Fig 4.8(b). The overall magnitude of I_{pc} follows the device conductance: decreasing from sweep 1 to 6 to 9, increasing from 9 to 12, and decreasing again from 12 to 13. While the images are not completely homogeneous (perhaps due to small differences in inter-facial contact across the junction), they do not show the characteristic domains formed during cooling or warming. To show this more explicitly, we have tracked I_{pc} at five different locations across the junction (see colored points in the lower image of Fig 4.8(c)), and their normalized change with drive number is shown in the lower panel of Fig 4.8(c) with the different traces offset for clarity. The photocurrent change for almost all locations uniformly follows the overall 1T-TaS_2 resistance. The only exception is the orange trace, showing slightly more saturated characteristics after sweep 9, which could be a consequence of a reduced current density or local electric field as this position is in the corner of the flake. This indicates that if CDW domains were created during electrical driving, their length scale should be much smaller than 1 μm, the laser spot size.

4.4 Free Energy Analysis of Electrically Driven NC-to-C Transition

The NC phase consists of C phase domains separated by a lattice of discommensuration (DC) lines that are presumably as metallic as the IC phase. The area density of DC's, n_{dc}, characterizes how similar the NC phase is to the C phase or IC phase. When n_{dc} equals $1/a^2$ (a: the lattice spacing), the system is in the IC phase, while when n_{DC} is zero, the system is in the C phase. Here, let us introduce a misfit parameter δ as :

$$\delta = \frac{n_{DC}.a^2}{M} \tag{4.1}$$

where M is the commensurability of the C phase, and M=3 in 1T-TaS_2. In terms of δ, we have

- C-phase: δ=0,
- IC-phase:δ=1/M,
- NC-phase: otherwise.

The volume fraction of the commensurate domain in the whole sample is given by,

$$v_c = 1 - n_{DC}.a^2 = 1 - M\delta. \tag{4.2}$$

We start from a Ginzburg-Landau free energy $F[\delta]$ calculated by Nakanishi and Shiba [40], which is schematically plotted in Fig 4.9 as the dashed line. The details of the functional form are not important for the following discussions; Ref. [40] provides further details. The main characteristic of the free energy is the existence of local minima at $\delta = 0$ (the C phase) and at δ=δ_{NC} (the NC phase). At a temperature slightly below the bulk transition temperature (as in the measurement shown in Fig 4.8 taken at 170K), the free energy of the C phase is lower than that of the NC phase, i.e., $F[0] < F[\delta_{NC}]$. The

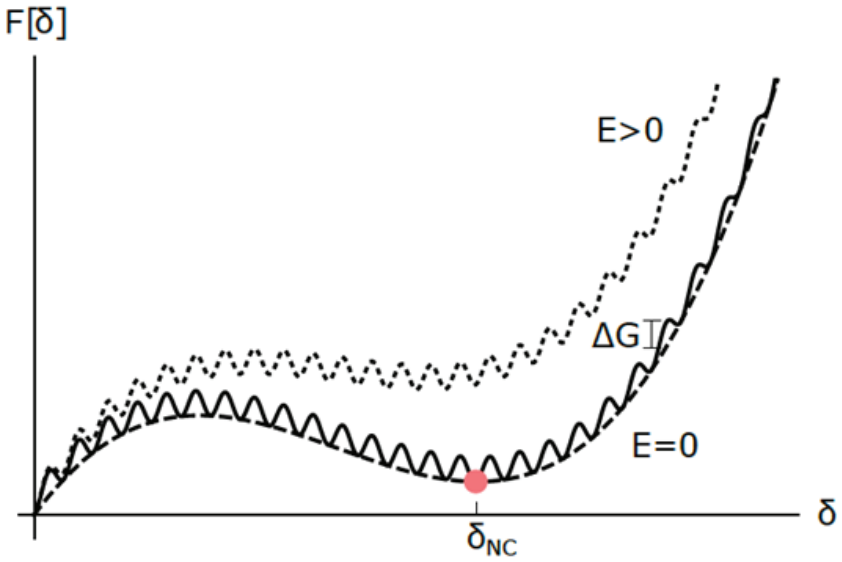

Figure 4.9: Ginzburg-Landau free energy for the charge-density wave order in 1T-TaS_2 as a function of misfit parameter δ. When the electric field E is absent, the C phase has a local minimum at $\delta = 0$, while the global minimum lies in the NC phase with $\delta_{NC} > 0$. The dashed line ignores the effect of the nucleation process of the discommensuration lines. The nucleation process with a potential barrier ΔG makes multiple local minima given by the solid line. The dotted line includes the effect of electric field E, which makes the nearly-commensurate phase less stable.

calculation was based on a model where δ can continuously change. However, the number of DC's can change only by a multiple of M, through the nucleation and annihilation process of a dislocation-antidislocation pair of DC's (see triplet figure, inset Fig 4.12 (a)). The detailed calculation for the energy of a dislocation-antidislocation pair is given in [23]; here, only the qualitative aspect is enough for the subsequent discussions. In Fig 4.9, we depicted the free energy, including this discreteness of DC's in the solid line, by adding an activation barrier potential ΔG between two δ's that differ by M=3.

Now we turn to the effect of the electric field on the free energy. In our experimental setup, the system is in a non-equilibrium steady state with currents flowing through the sample. We will not consider the kinetic energy of the currents since they are dissipating into the substrate, and the effect of heating is negligible in experiments. We will treat the effect of electric fields only phenomenologically by assuming that the commensurate domain is dielectrically harder than the DC part [22]. The assumption is based on the fact that the commensurate domain is insulating, while the DC's are metallic as in the IC phase. Let us write the polarization of the commensurate domain per volume as P_0, and ignore the polarization in the DC part. Then the energy density due to the polarization is given by

$$F_p = -v_c.P_0.E = -(1 - M\delta).P_0.E \tag{4.3}$$

where v_c is the volume fraction of the commensurate domain in the whole sample.

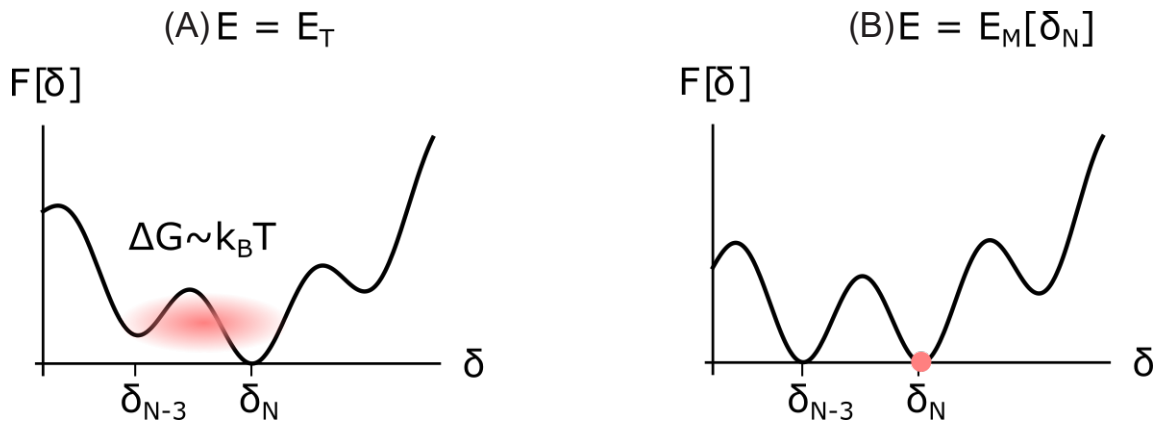

Figure 4.10: Two characteristic electric fields E_T and E_M. (A) At E=E_T, the thermal transition from δ_N to δ_{N-3} is activated. (B) For $E_M[\delta_N]$, the local minimum at δ_{N-3} becomes equal in energy to that at δ_N, where the system is originally located.

The term proportional to Eδ tilts the free energy curve and makes the NC phase less stable (the dotted line in Fig 4.9). In Fig 4.10, we depict the two characteristic electric fields E in the process of transition from a local minimum at δ_N with N DC lines to the adjacent one at δ_{N-3} with (N-3) DC lines. The first characteristic field $E_T[\delta_N]$ is the critical field that makes the energy activation barrier ΔG between δ_N and small enough for the thermal activation process, i.e., $\Delta G \sim k_B T$. We expect that this critical field is only weakly dependent on δ, thus we assume a constant E_T in the following analysis. The second characteristic field, $E_M[\delta_N]$, is defined by the field, at which the free energy at δ_N becomes larger than the one at the adjacent minimum at δ_{N-3}, i.e., $F[\delta_{N-3}] < F[\delta_N]$. If this inequality is not satisfied, the system is likely to go back to the original minimum δ_N. Near the local minimum at δ_{NC} in Fig 4.9, the free energy is concave up (the curvature is positive), and thus a larger critical field E_M is required as δ becomes smaller,

$$E_M[\delta_N] < E_M[\delta_{N-3}] < E_M[\delta_{N-6}] < \cdots . \tag{4.4}$$

Depending on the temperature T, the activation potential height ΔG, and the overall shape of the free energy $F[\delta]$, there are two possible scenarios regarding the two critical field values: (a) $E_M[\delta] > E_T$ or (b)$E_M[\delta] < E_T$.

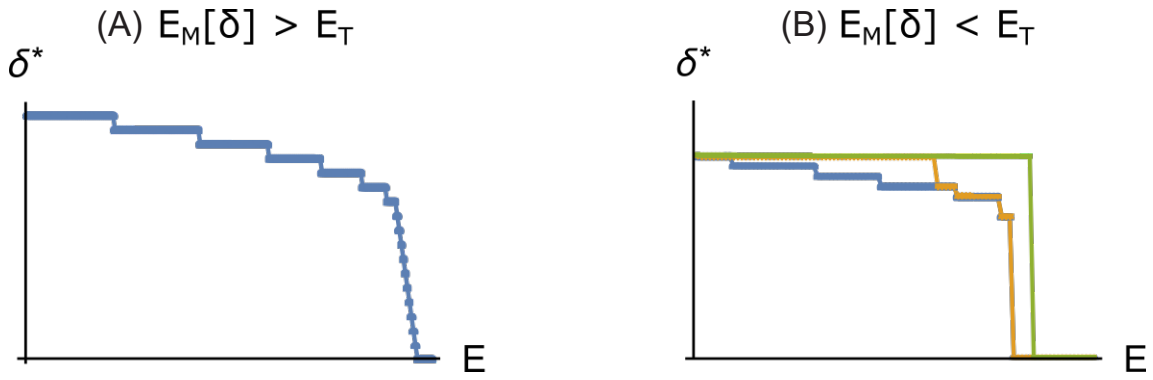

Figure 4.11: The transition of δ in the two scenarios as the electric field E is adiabatically increased. (A) When $E_M[\delta] > E_T$, the system experiences consecutive stepwise jumps between adjacent local minima, until crossing over the large peak and rushing into the commensurate phase. (B) When $E_M[\delta] < E_T$, nonconsecutive jumps occur. When E_T is small (blue line), the step of the jumps is still one or two. As E_T increases, the step of the jump becomes larger (orange line), and even a direct transition to the commensurate phase is possible (green line).

In scenario (a), as we increase the electric field, the thermal activation process first becomes possible at $E = E_T$. However, the local minimum at δ_{N-3} only becomes more stable at $E = E_M[\delta_N]$, leading to the transition $\delta_N \to \delta_{N-3}$. As we further increase E, consecutive step-wise jumps to adjacent local minimum occur ($\delta_{N-3} \to \delta_{N-6} \to \cdots$) as the electric field passes threshold values, $E_M[\delta_{N-3}], E_M[\delta_{N-6}], \cdots$ (Fig 4.11(a). At a large enough field value, the system will even transition fully to the C phase if the large peak between the C phase and the NC phase can be overcome energetically. In scenario (b), for$E_M[\delta] < E_T$, the local minimum at δ_N becomes metastable, and the one at δ_{N-3} becomes

more stable. However, due to the activation barrier in between, the system remains in the metastable state at δ_N. As E further increases, the location of the stable minimum shifts incrementally: $\delta_{N-3} \rightarrow \delta_{N-6} \rightarrow \delta_{N-9}$..... At E=$E_T$, the thermal activation process is enabled, and a non-consecutive jump to the new stable minimum occurs: $\delta_N \rightarrow \delta_{N-3p}$, where p is an integer (the orange line in Fig 4.11(b)). If the activation barrier between adjacent minima is very high or the energy difference between the NC phase and the C phase is small at E=0, it is even possible for the system to directly jump to the C phase (the green line inFig 4.11(b)). The scenario with small or moderate value of E_T qualitatively explains our observations of discrete jumps in the I-V curves. We expect that the abrupt first-order-like switching near $E \sim E_c$ is caused by the nonlinear coupling between δ and E , which is, however, beyond the scope of our model.

4.5 Discussion

In this section we discuss the relevance of the phenomenological model presented in the previous section in explaining the observed homogeneous switching. While the NC-to-C transition proceeds in multiple steps, the reverse transition is abrupt. This likely reflects different origins for the two, and so we discuss the forward and backward transitions separately.

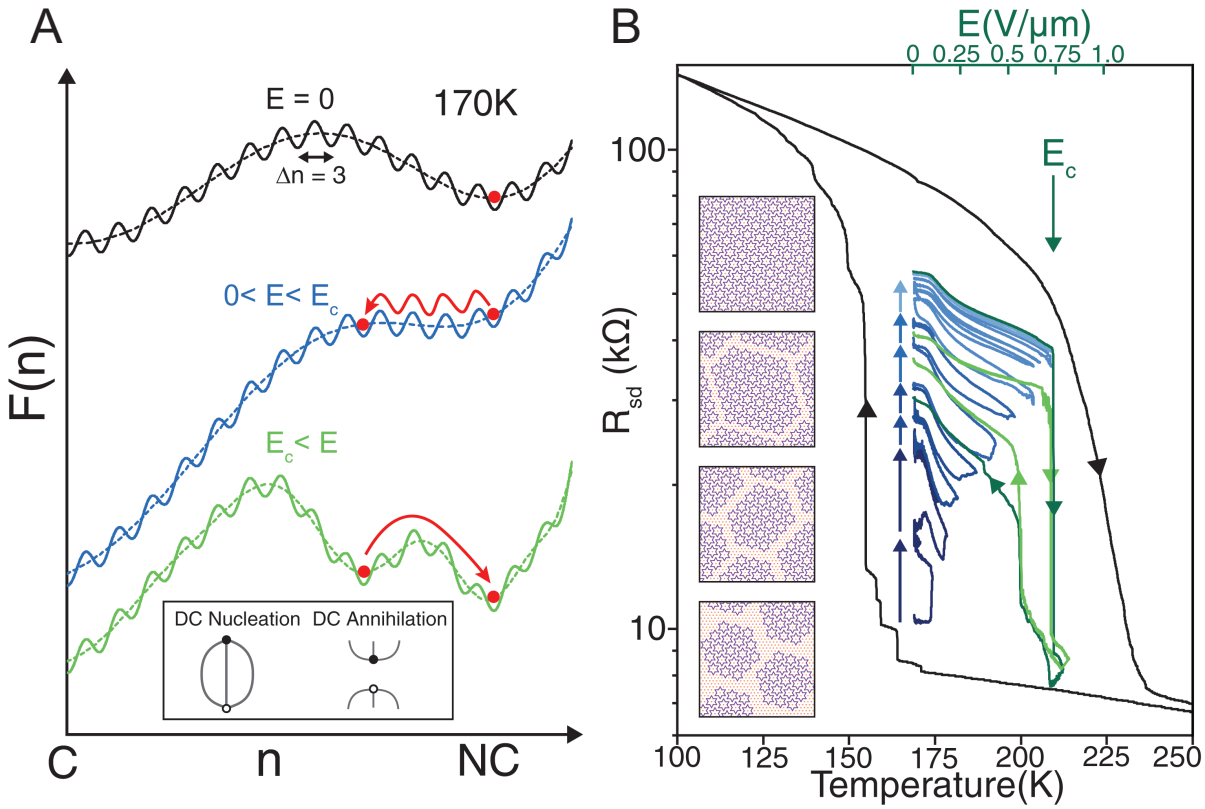

Figure 4.12: Proposed mechanism for bidirectional switching. (A) Free energy schematic visualizing the effect of applied electric field E at 170 K with discommensuration (DC) density n as the order parameter. The dashed lines represent the overall energy landscape, and oscillations correspond to the discrete annihilation and creation of triplet DCs (see bottom-left inset). (B) 1T-TaS_2 resistance versus temperature and electric field for the sweeps shown in Fig4.8(A) showing the difference between forward and reverse transitions and metastable resistance states accessed. The schematics in the inset show growing C domains with increasing R_{sd} in accordance with our model.

A conducting network of discommensurations (DCs) distinguishes the NC phase from

the C phase,[43] [74][73][7] [59] and so the areal density of DCs, n_{DC}, can be used as an order parameter to describe the energetics of the NC-C transition[40] with n_{DC} being zero (nonzero) in the C (NC) phase. The free energy landscape describing the initial state is shown by the black trace in the main panel of Fig4.12(a). At 170 K, the C phase is the thermodynamic ground state; however, the sample remains locked in the local NC minimum due to the activation barrier. Importantly as show n_{DC} in the previous section, the energy is not a smooth function of n_{DC}, as DCs must be nucleated and annihilated discretely in triplets in 1T-TaS_2 in order to conserve the phase around a CDW dislocation.[23],[37] These two processes are illustrated in the inset in Fig4.12(a), where the triplet DCs (represented by lines) are shown to terminate at a pair of dislocations (represented by filled and open circles). As the DCs are more conducting than the C regions, the latter can be more highly polarized by an external electric field, E.[22] Applying a finite E below a critical value, E_c, then lowers the energy more for states with smaller n, thus tilting the energy landscape to destabilize the NC state, as shown by the blue trace in 4.12(a). For a given n, the energy further decreases linearly with E. This allows the system to gradually transition toward the C phase by traversing a series of local, metastable minima corresponding to a decreasing density of DCs.

This qualitatively captures the multistep NC-to-C transitions observed in our experiment, which are summarized in Fig 4.12(b). Here, we have overlaid the temperature-dependent resistance R_sd (in black) for the 5-8 nm thick device and R_sd versus electric field E (top x-axis) at 170 K corresponding to the forward driving (in blue) from Fig4.8(a) for comparison. Applying relatively small fields in the NC phase allows access to multiple metastable states within the hysteresis region of the temperature-driven transition, which in light of our analysis and imaging we now interpret as an incremental melting of the NC DC network that is distributed relatively uniformly across the sample (see insets in Fig 4.12(b)). When the system is near the C phase with higher resistance, application of $E > E_c \sim 0.7V/\mu$m causes an abrupt reverse transition back toward a lower resistance state. The green traces in Fig 4.12(b) show two instances of this backward driving for comparison. In both cases, the 1T-TaS_2 resistance immediately after this transition is

very close to that of the NC phase at higher temperature under equilibrium conditions, and so we have drawn the energy landscape in green in Fig 4.12(a) to describe this state phenomenologically. The overall activation barrier between the starting and final states reflects the hysteresis between ramping field up and down, which is caused by a first-order phase transition. This may indicate additional nonlinear coupling between E and n that is beyond the scope of our model. Nonetheless, the original NC DC network is nucleated again in this free energy picture, resetting the system. The melting process is active again when ramping the field back to zero, however, which leaves the system in an intermediate state.

Abrupt voltage/current-induced transitions from the C phase into CDW states with higher conductivity have been previously observed under various conditions. In lateral devices with in-plane currents and fields, it has been attributed to a carrier-driven breakdown of the insulating state,[24] as well as to the formation of conducting, textured domains,[68] althoughJoule heating is also possible.[75] Indeed, mosaic-like metallic domains have been induced on bulk 1T-TaS_2 using the tip of a scanning tunneling microscope by modifying the natural inter-layer stacking.[35] [12] However, the electric fields used in these studies are orders of magnitude larger than our E_c which suggest a different mechanism. The NC resistance we observe above E_c is also inconsistent with that of a random domain network. If the transition was instead induced by Joule heating above the warming transition temperature, we then expect through subsequent cooling as the voltage is ramped down that CDW domains would appear similar to that for the temperature-driven transition shown in Fig 4.6. The photocurrent images taken afterward are also inconsistent with this scenario and thus point to other possibilities, such as a carrier-driven breakdown of the C phase, although the possibility of electrically induced changes in inter-layer stacking cannot be strictly eliminated.

Chapter 5

Infrared microscopy of High Pressure Hydrides

Bardeen–Cooper–Schrieffer (BCS) theory explains the superconductive phenomena by pairing of electrons in a net attractive potential. [3] In conventional superconductors this attractive potential is created by electron-phonon interactions. Thus there is no theoretical upper bound on the superconducting transition temperature T_C, that is if the right conditions for the electron-phonon interactions are met.

In 1968 Ashcroft predicted that high-pressure hydrogen would be a high-temperature superconductor due to three main arguments : (1) the light proton mass allows for high frequency phonons. (2) simple coulomb interaction between electron-ion should provide a strong electron-phonon coupling.(3) At high pressure the electronic DOS at the Fermi surface should be large. [1] Further calculations that showed that metallic hydrogen would be a superconductor at ∼300-350K in the atomic crystalline phase around 500GPa.[36] However superconductivity in pure hydrogen has not been found mainly due to the extreme pressure requirement. The focus has since shifted onto hydrogen dominated materials.

H_2S was predicted to transform to a metal and a superconductor at a lower (and experimentally achievable) pressure of P≈100GPa and a high T_C≈80K.[32] Other materials

with higher hydrogen content such as YH_{10} and LaH_{10} were predicted to have T_C's of 303K and 280K at 400GPa and 200Gpa respectively.

In this chapter the first section briefly describes the diamond anvil cell (DAC) that is used to fabricate these samples under these extraordinary pressures. Section 2 shows the superconductivity transitions observed in H_3S [33] and LaH_x [47] samples. Changes in the reflectivity of H_3S samples in the near-IR region that motivate our scanning laser measurements in the same spectral region are shown in section 3. Section 4 shows the preliminary data obtained by scanning laser microscopy with laser wavelength of 2300nm on a superconducting H_3S samples.

5.1 Crystal Synthesis

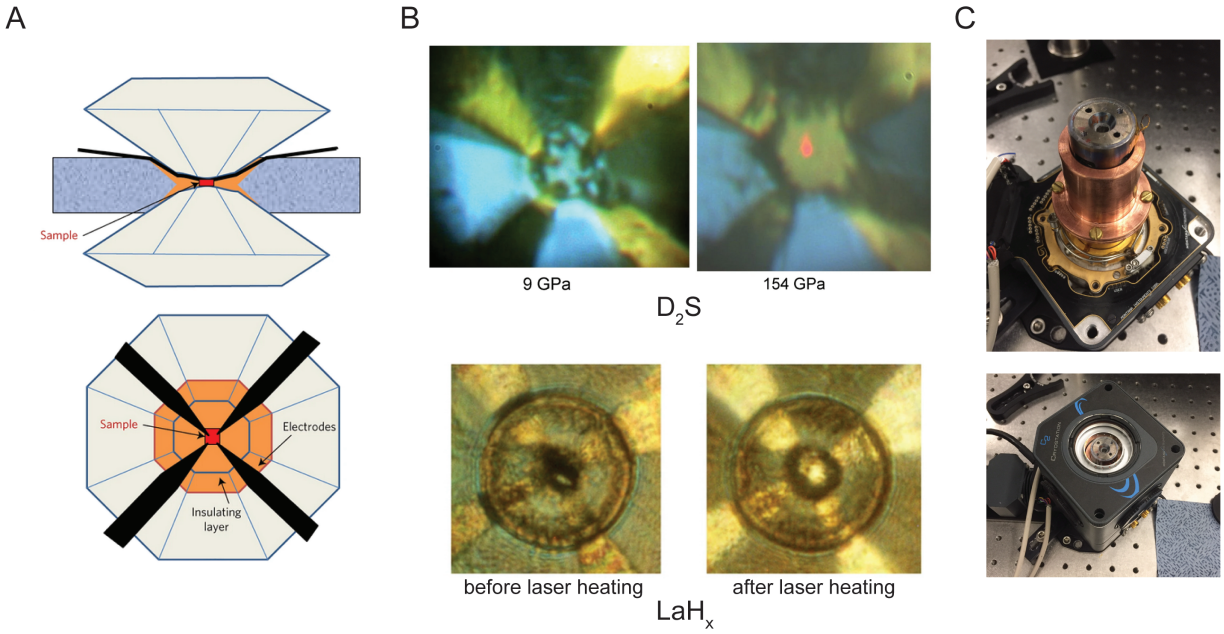

Figure 5.1: Metallic hydrides fabricated inside diamond anvil cells (DAC). (A) Schematic of a typical diamond anvil cell consists of a gasket (blue) squeezed between two diamonds. The sample (red) is packed inside an insulating slat layer (orange) which fills a central hole in the gasket. One of the diamond (top) has sputtered electrodes (Pt) that allow for electrical measurements. (B) Fabrication of a metallic sulfur deuteride(top) and Lanthanum hydride (bottom) systems at high pressures. The Lanthanum crystals require additional laser heating to induce the transition. (C) A DAC loaded onto the C2 cryostat for optical measurements without (top) and with (bottom) the outer covering. Figure (A) taken from [10], Figure (B, top) taken from [15] Figure (B, bottom) taken from [14]

High pressures required to fabricate the predicted hydirdes is achieved by compressing the precursor materials between two diamond anvils. Fig.5.1(A) shows the schematic of a typical diamond anvil cell or DAC. A stainless steel gasket (blue) is used to hold the sample

in the middle. The region inside the center is packed with an insulating salt such as NaCl or $CaSO_4$ (orange) that prevents shorting of electrodes, which are usually sputtered onto one of the diamond anvils and also do not react with the sample materials. The sample region is shown colored in red.

For the fabrication of H_3S samples H_2S gas is introduced into the sample space at $\sim$200K. Then the pressure is increased, Raman spectra of the sample region is monitored simultaneously and changes in characteristic vibrational peaks signify structural phase transitions. For $\approx$100GPa the samples becomes metallic and shows superconducting transition with T_C <100K. Fig.5.1 (B) top, shows the sample formation as the region in center goes from transmitting to opaque upon increase in pressure. Further increase in pressure and and repeated annealing between room and low temperatures stabilizes the superconducting transition.

Fabrication of superconducting LaH_{10} a little more complex. Precursor elements involve pure La which is put into the sample space together with an excess of hydrogen and the pressure is increased to 120-190GPa. The sample region is then heated to make the precursors react with one-sided pulsed radiation form a YAG laser focused onto a spot of diameter $\sim 10\mu$m. The sample is heated to $\sim$1000K and various LaH_x compounds are formed. In hydrogen deficient environment LaH_3 is predominantly formed which is also used as a precursor for fabrication of some samples. Fig.5.1(B) bottom show La + H_2 samples before and after laser heating. X-ray diffraction is used to determine the structural phase at the local level. for samples with LaH_{10} the T_C of 250K has been reported.

Resistivity measurements that show the superconductivity transition in these samples is discussed in the next section. Further information on these samples is obtained by optical measurements done through the top diamond. We use aim to use our scanning laser setup to map the spatial evolution of reflection at a particular wavelength. Fig.5.1(C) shows a typical DAC mounted on our Montana C2 cryostat for such optical measurements. Bottom image shows the sample with the protective shielding and the outer cover at a very low temperature <100K.

5.2 Superconductivity Transition : T_C

The most direct way measuring superconductivity in the samples fabricated from the process shown above is observing the characteristic drop in resistivity to 0 at the superconducting transition. This is measured using a standard van-der-pauw geometry of electrodes shown in Fig.5.1(A) (bottom).

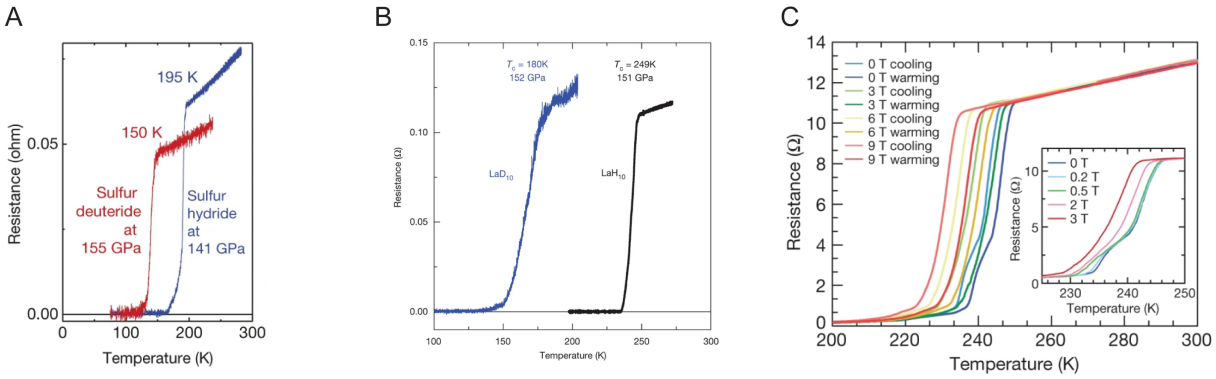

Figure 5.2: Superconductivity transitions in high pressure hydrides. (A) Typical superconductive steps for sulfur hydride (blue) and sulfur deuteride (red) taken during a slow warm-up. (B) Superconductive transitions in LaH_{10} and LaD_{10} samples. For both the class of compounds deuteride samples show a marked lowering of T_C. (C) Superconducting transitions under warm-up and cool-down for applied magnetic field in LaH_{10} samples reduces the onset of superconductivity. A notable step observed in the zero field transition is removed for fields above 3T (inset). Figure (A) taken from [15], Figure (B), (C) taken from [14]

For the H_3S samples the superconducting drop in resistivity can be seen can be seen after pressures above 107GPa. The T_C increases with increasing pressure but initially pressurized samples show a varying T_C upon separate thermal cycles. Multiple cycles of thermal annealing between room-temperature and 100K stabilizes the T_C. Fig.5.2(A) shows the

transition in thermally annealed Sulfur deuteride and Sulfur hydride samples upon warm-up form 100K at the pressures of 155GPa and 141 GPa respectively. The isotope effect is observed : T_C is lowered for deuteride samples indicating phonon-assisted superconductivity. The same effect is seen in Lanthanum hydride samples shown in Fig.5.2(B).

The other proof of superconductivity is the Meissner effect which is the complete expulsion of the magnetic field from the sample after the superconducting transition which is very hard to measure for sample under such pressures. The reduction in T_C dues to an applied magnetic field (Fig. 5.2(C)) does indicate the superconducting nature of the transition, The two step transition at 0 field (highlighted in inset) also disappears as the T_C lowered for magnetic fields of 3T and larger. This behavior is consistent for in-homogeneous superconducting samples and is seen for samples at ambient pressures. Note that some in-homogeneity is inevitable for samples fabricated at high pressures due to pressure and elemental in-homogeneity.

5.3 Bosonic Reflection Spectrum

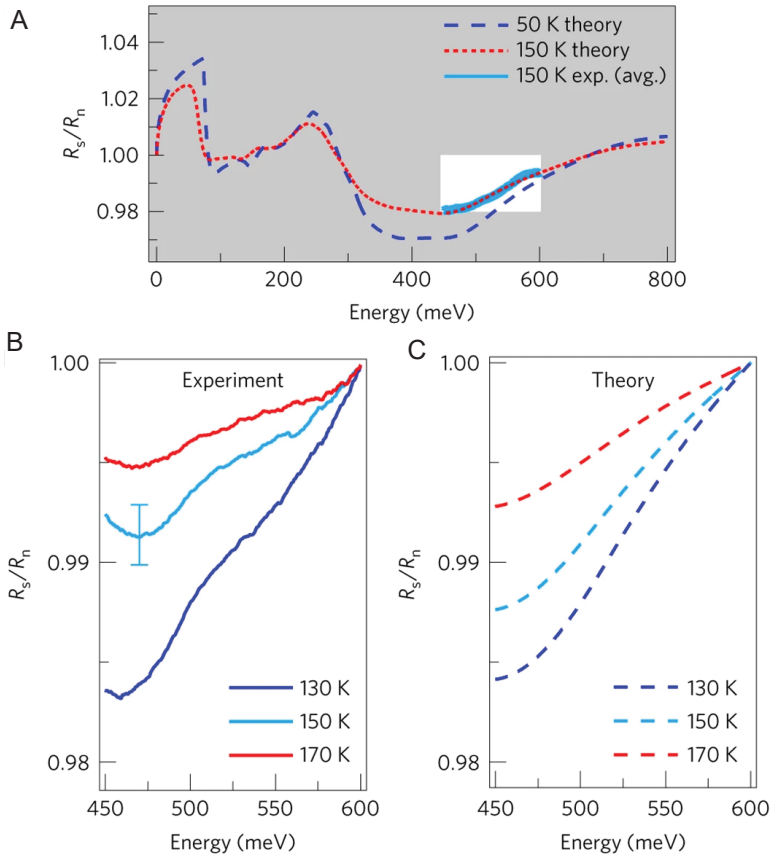

Figure 5.3: Reflection spectrum of superconducting hydrides. (A) Normalized reflectivity calculated for a superconductive sample in the dirty limit normalized by the value at 200K in the normal state. Experimentally data is overlaid for the region in the white box. (B) Reflection spectrum measured at different temperatures normalized to the value at 600meV. (C) Calculated spectrum for the same temperatures. Figure taken from [10]

While a direct measurement of the Meissner effect remains a challenge, reflectance measurements are a viable alternative to explore the physics of these samples. Reflectivity

measurements done on the H_3S samples [10] have been shown to be in agreement with theoretical predictions based on DFT and Migdal–Eliashberg theory. A superconductor is a perfect reflector of light upto the photon energy of $\hbar\omega = 2\Delta$ where Δ is the superconducting gap. Above this energy the reflection is determined by the optical scattering rate. Calculated reflection spectrum of H_3S reveals three regions of interest in this regard. The superconducting gap region lies between 65 to 100 meV. Between 100 to 200 meV reflection is reduced due to scattering by optically active phonons ($\hbar\Omega \sim 200$ meV) and the region between 350-500 meV ($2\Delta + \hbar\Omega$) where the reflection is reduced strongly by scattering due to Bosonic excitation. The reflection is additionally effected by the purity of the sample. If the electron mean free path (l) is greater than the superconducting coherence length (ξ) then superconductor is said to be in the clean limit. If the amount of impurities in the superconductor is high such that it reduces l of the regular metal lower than ξ then the superconductor is said to be in the dirty limit. In the dirty limit, scattering rate of electrons is larger than 2Δ [27] which directly effects the ratio of reflectivity between the normal and superconducting state close to 2Δ. Thus the first two features in the reflection spectrum discussed before are more pronounced when the sample is in the dirty limit. For our laser based measurements we are interested in the 450 to 600 meV region where boson assisted scattering will reduces the reflectance of the sample.

Fig.5.3(A) shows the calculated normalized reflection spectrum of a dirty superconductor with a $T_C = 200$K at 50K and 150K. The curve is normalized with the normal state at 200K. The change in the reflection of the depression around 400 meV for lower temperatures is quite evident. The white box represents the spectral region for which measured data (in blue) is plotted. Fig.5.3(B) shows the thermal evolution of the reflectance in this spectral region where the plots are normalized to the value at 600meV. Theoretical predictions for the same are shown in the Fig.5.3(C).

Motivated by this result we choose a laser wavelength of 540 meV (2300 nm) to use with our scanning laser setup to map the spatial evolution of the superconducting transition as a function of temperature. In the next section we present initial results of such measurement which should hope to work as proof of principle for such measurements in the future.

5.4 IR Laser Scanning : early results

The spatial in-homogeneity of the high-pressure hydrides can be mapped at the structural level using X-ray diffraction measurements [14]. But an active measurement of onset of superconductivity can be measured using reflectivity.

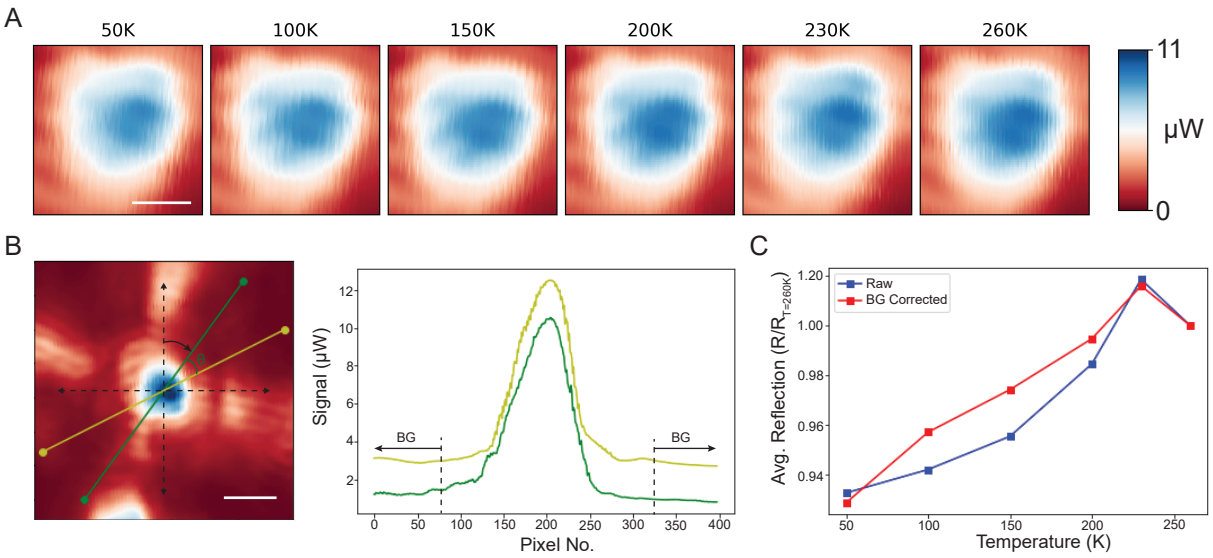

Figure 5.4: IR laser reflection microscopy of high-pressure hydrides. (A) Zoomed in reflection image of H_3S sample taken using a 2300 nm laser at temperatures across the superconducting transition temperature. Scale bar in the first panel is 10 μm. (B) Zoomed out image(left) taken at 260K showing the metal electrodes.Scale bar is 20 μm. Line cuts taken at an angle are selected to obtain the uniform background(BG) signal shown in the left panel(offset for clarity). BG signal obtained by averaging over the region in between light and dark green line cuts which is subtracted to perform correction. (C) Normalized reflection obtained by averaging over the region in (A), Raw(blue) and BG corrected(red) and divided by the value at T = 260K.

By careful selection in 450 to 600meV energy range which avoids both atmospheric and

diamond absorption we choose laser of 2300nm(540meV) wavelength. We also modifying the scanning laser optical setup to have CaF_2 lenses and the C2 cryostat to have a CaF_2 optical window in order to get the best transmission for the selected wavelength. Since the sample is located ∼15 mm bellow the top surface of the optical window we use a 15x Schwarzschild objective (N.A. = 0.5) with a working distance of 23mm which allows the sample to come into focus at the lowest temperatures. To optimize the signal to noise ratio the diode laser is electronically modulated using a lock-in and the reflection signal is collected at the same frequency. We get a signal of few a μW with a dark -room signal of ∼nW. There is an additional problem of change in focal plane between temperatures which is solved by taking multiple images across various points on the z-axis and selecting for maximal signal from the sample region.

Fig.5.4 shows the reflection scans taken on a H_3S sample with pressure of 148GPa (H2 vibron) and a T_C = 196K upon cooldown. Fig.5.4(B) shows a typical image in which reflection signal from both the sample region(center) and the electrodes is visible(vertical and off-axis horizontal to the side). Fig.5.4(A) shows the cropped out images of the sample region taken at various temperatures. Averaging the signal over this region and normalizing it to the signal at 260K we see that the average reflectivity of the sample starts to decrease after 230K(blue trace Fig.5.4(C)). In order to correct for the background signal which is caused due to reflections of the diamond we select another region which should have constant reflectivity. That is the region without the electrodes or the sample. We take a off-axis line-cut across the sample Fig.5.4(B) (in green) and select the regions with a flat signal profile that is upto 75 pixel number and beyond 325 pixel number Fig.5.3(B) (left). Averaging this region to determine the background at each temperature we subtract it from the raw data of the line cut before averaging. Plot for the background corrected data is shown in the red-curve in Fig.5.4(C). This preliminary result shows a reduction in the overall reflectivity of the sample staring at a temperature close to onset of superconductivity as measured by the resistance data. This is in agreement with the expected trend and previous experimental results. Further data taken at more closely spaced temperatures would give a more robust data set on which more rigorous BG correction can be

done. Once established the can be used as a tool to establish bosonic nature of the superconducting transition and map spatial inhomogeneity in such samples. This will be more relevant to other systems where laser heating is an added step to the fabrication process. Inhomogeneity can arise due to uneven distribution of precursor material, pressure or heat (as applied by a laser).

Chapter 6

Summary and Outlook

6.1 Summary

In summary, a laser scanning optical setup coupled with a 4K cryostat was assembled. It can be used to raster a diffraction limited laser spot with wavelengths ranging from 450nm to 8μm. We used it to study spatial distribution of two correlated electron phases with light of 520nm and 2300nm respectively.

The first material we studied is 1T-TaS_2 which is a CDW material. We proposed a novel device geometry which utilizes the recent advances made in fabrication of 2-D Vander-Waals heterostructures. After establishing the proof of principle we used such devices to map the NC-C transition while changing 3 key parameters, 1T-TaS_2 flake thickness, temperature and applied electric field. For the thermally driven transitions we showed that NC to C transition is slowed down in ultra-thin flakes in comparison to the bulk-like thickness with clear formation of micron sized domains some of which remain frozen in the NC phase at low temperatures. This is in contrast to the electrically driven transitions where we do not see formation of domains down to the micron limit in states with intermediate resistance values. Additionally, we show for the first time bi-drectional electrical driving at a constant temperatures in ultra-thin flakes while accessing multiple states of

intermediate resistance. We also present the phenomenological model of the multi-step NC to C electrical driving which is based on previous experimental and theoretical work done to describe the complex dynamics of the NC phase.

The second material studied is superconductive H_3S under a very high pressure of $\sim$150GPa. Previous experiments reveal a drop in reflectivity in the near-IR spectral region which had been theoretically predicted to arise from the bosons in the superconductive phase. We obtain reflection images of the sample in this spectral range and show that average reflectivity follows the theoretically predicted model.

6.2 Outlook

The results obtained for 1T-TaS_2 reveal important differences in the spatial dynamics of thermally and electrically driven flakes. The spatial uniformity of electrically driven transition allows the possibility of device miniaturization. The multi-step NC to C transition and the ability for bi-directional driving improves the case for use of 1T-TaS_2 as a reversible multi-state-memristor material in the future. Additionally, the origin of the first-order C to NC transition observed at high applied electric field remains to be investigated. A better understanding of this transition would allow for a much robust control of the intermediate states.

Early results of reflection mapping the superconductivity transitions in H_3S agree well with the theoretical predictions. [11] Recently room-temperature superconductivity has been reported in a similar Carbonaceous Sulfur Hydride system.[54] The experimental setup described in this thesis will be an added tool to probe these exotic materials and would help to establish the nature of superconductivity in these samples. And would also help the fabrication process by identifying the distribution of the superconducting phase in relation to the crystalline phase identified using x-ray diffraction.

References

[1] N. W. Ashcroft. Metallic hydrogen: A high-temperature superconductor? *Phys. Rev. Lett.*, 21:1748–1749, Dec 1968.

[2] N. W. Ashcroft. Hydrogen dominant metallic alloys: High temperature superconductors? *Phys. Rev. Lett.*, 92:187002, May 2004.

[3] J. Bardeen, L. N. Cooper, and J. R. Schrieffer. Theory of superconductivity. *Phys. Rev.*, 108:1175–1204, Dec 1957.

[4] J.G. Bednorz and K.A. Müller. Possible high T_c superconductivity in the Ba-La-Cu-O system. *Zeitschrift fur Physik B Condensed Matter*, 64:189–193, June 1986.

[5] P. Blake, E. W. Hill, A. H. Castro Neto, K. S. Novoselov, D. Jiang, R. Yang, T. J. Booth, and A. K. Geim. Making graphene visible. *Applied Physics Letters*, 91(6):063124, 2007.

[6] L. Britnell, R. M. Ribeiro, A. Eckmann, R. Jalil, B. D. Belle, A. Mishchenko, Y.-J. Kim, R. V. Gorbachev, T. Georgiou, S. V. Morozov, A. N. Grigorenko, A. K. Geim, C. Casiraghi, A. H. Castro Neto, and K. S. Novoselov. Strong light-matter interactions in heterostructures of atomically thin films. *Science*, 340(6138):1311–1314, 2013.

[7] B. Burk, R. E. Thomson, A. Zettl, and John Clarke. Charge-density-wave domains in 1T-TaS_2 observed by satellite structure in scanning-tunneling-microscopy images. *Phys. Rev. Lett.*, 66:3040–3043, Jun 1991.

[8] C. Butler, M. Yoshida, T. Hanaguri, and Y. Iwasa. Mottness versus unit-cell doubling as the driver of the insulating state in 1t-tas2. *Nature Communications*, 11, 2020.

[9] C. J. Butler, M. Yoshida, T. Hanaguri, and Y. Iwasa. Doublonlike excitations and their phononic coupling in a mott charge-density-wave system. *Phys. Rev. X*, 11:011059, Mar 2021.

[10] F. Capitani, B. Langerome, Jean-Blaise Brubach, Pascale Roy, A. Drozdov, M. Eremets, E. Nicol, J. Carbotte, and T. Timusk. Spectroscopy of H_3S: evidence of a new energy scale for superconductivity. *Nature Physics*, 13, 12 2016.

[11] J. P. Carbotte, E. J. Nicol, and T. Timusk. Detecting superconductivity in the high pressure hydrides and metallic hydrogen from optical properties. *Phys. Rev. Lett.*, 121:047002, Jul 2018.

[12] Doohee Cho, Sangmo Cheon, Ki-Seok Kim, Sung-Hoon Lee, Yong-Heum Cho, Sang-Wook Cheong, and Han Woong Yeom. Nanoscale manipulation of the Mott insulating state coupled to charge order in 1T-TaS_2. *Nature Communications*, 7:10453, January 2016.

[13] F.J. Di Salvo and J.E. Graebner. The low temperature electrical properties of 1T-TaS_2. *Solid State Communications*, 23(11):825–828, 1977.

[14] A. P. Drozdov, P. Kong, V. S. Minkov, S. Besedin, M. A. Kuzovnikov, S. Mozaffari, L. Balicas, F. Balakirev, D. Graf, V. Prakapenka, E. Greenberg, D. Knyazev, M. Tkacz, and M. Eremets. Superconductivity at 250 k in lanthanum hydride under high pressures. *Nature*, 569:528–531, 2019.

[15] A.P. Drozdov, M.I. Eremets, I.A. Troyan, V. Ksenofontov, and S.I. Shylin. Conventional superconductivity at 203 kelvin at high pressures in the sulfur hydride system. *Nat*, 525(7567):73–76, sep 2015.

[16] Maximilian Eichberger, Hanjo Schafer, Marina Krumova, Markus Beyer, Jure Demsar, Helmuth Berger, Gustavo Moriena, German Sciaini, and R.J. Dwayne Miller. Snapshots of cooperative atomic motions in the optical suppression of charge density waves. *Nat*, 468(7325):799–802, December 2010.

[17] Yuqiang Fang, Jie Pan, Jianqiao He, Ruichun Luo, Dong Wang, Xiangli Che, Kejun Bu, Wei Zhao, Pan Liu, Gang Mu, Hui Zhang, Tianquan Lin, and Fuqiang Huang. Structure re-determination and superconductivity observation of bulk 1T-MoS_2. *Angewandte Chemie International Edition*, 57(5):1232–1235, 2018.

[18] Alex J. Frenzel, Alexander S. McLeod, Dennis Zi-Ren Wang, Yu Liu, Wenjian Lu, Guangxin Ni, Adam W. Tsen, Yuping Sun, Abhay N. Pasupathy, and D. N. Basov. Infrared nanoimaging of the metal-insulator transition in the charge-density-wave van der waals material 1T-TaS_2. *Phys. Rev. B*, 97:035111, Jan 2018.

[19] Herbert Fröhlich. On the theory of superconductivity: the one-dimensional case. *Proceedings of the Royal Society of London. Series A. Mathematical and Physical Sciences*, 223(1154):296–305, 1954.

[20] Andre K. Geim and K. Novoselov. The rise of graphene. *Nature materials*, 6 3:183–91, 2007.

[21] George Grüner. *Density Waves in Solids*. CRC Press, first edition, 1994.

[22] K. Hamano, H. Sakata, and K. Ema. Kinetic process of formation of discommensuration lattice in the first-order commensurate-incommensurate transition. *Ferroelectrics*, 137(1):235–250, 1992.

[23] Rui He, Junichi Okamoto, Zhipeng Ye, Gaihua Ye, Heidi Anderson, Xia Dai, Xianxin Wu, Jiangping Hu, Yu Liu, Wenjian Lu, Yuping Sun, Abhay N. Pasupathy, and Adam W. Tsen. Distinct surface and bulk charge density waves in ultrathin 1T-TaS_2. *Phys. Rev. B*, 94:201108, Nov 2016.

[24] Matthew J. Hollander, Yu Liu, Wen-Jian Lu, Li-Jun Li, Yu-Ping Sun, Joshua A. Robinson, and Suman Datta. Electrically driven reversible insulator–metal phase transition in 1T-TaS_2. *Nano Letters*, 15(3):1861–1866, 2015. PMID: 25626012.

[25] Tatsuhiko Ikeda, Hirokazu Tsunetsugu, and Kenji Yonemitsu. Photoinduced dynamics of commensurate charge density wave in 1t-tas2 based on three-orbital hubbard model. *Applied Sciences*, 9:70, 12 2018.

[26] R. Inada, Y. Ōnuki, and S. Tanuma. Hall effect of 1T-TaS_2. *Physics Letters A*, 69(6):453–456, 1979.

[27] K. Kamarás, S. L. Herr, C. D. Porter, N. Tache, D. B. Tanner, S. Etemad, T. Venkatesan, E. Chase, A. Inam, X. D. Wu, M. S. Hegde, and B. Dutta. In a clean high-t_c superconductor you do not see the gap. *Phys. Rev. Lett.*, 64:84–87, Jan 1990.

[28] Hyun Ho Kim, Bowen Yang, Tarun Patel, Francois Sfigakis, Chenghe Li, Shangjie Tian, Hechang Lei, and Adam W. Tsen. One million percent tunnel magnetoresistance in a magnetic van der waals heterostructure. *Nano Letters*, 18(8):4885–4890, 2018. PMID: 30001134.

[29] W. Kohn. Image of the fermi surface in the vibration spectrum of a metal. *Phys. Rev. Lett.*, 2:393–394, May 1959.

[30] Sung-Hoon Lee, Jung Suk Goh, and Doohee Cho. Origin of the insulating phase and first-order metal-insulator transition in $1t-tas_2$. *Phys. Rev. Lett.*, 122:106404, Mar 2019.

[31] L. J. Li, W. J. Lu, X. D. Zhu, L. S. Ling, Z. Qu, and Y. P. Sun. Fe-doping–induced superconductivity in the charge-density-wave system 1T-TaS_2. *EPL (Europhysics Letters)*, 97(6):67005, mar 2012.

[32] Yinwei Li, Jian Hao, Hanyu Liu, Yanling Li, and Yanming Ma. The metallization and superconductivity of dense hydrogen sulfide. *The Journal of Chemical Physics*, 140(17):174712, 2014.

[33] Hanyu Liu, Ivan I. Naumov, Zachary M. Geballe, Maddury Somayazulu, John S. Tse, and Russell J. Hemley. Dynamics and superconductivity in compressed lanthanum superhydride. *Phys. Rev. B*, 98:100102, Sep 2018.

[34] Y. Liu, R. Ang, W. J. Lu, W. H. Song, L. J. Li, and Y. P. Sun. Superconductivity induced by se-doping in layered charge-density-wave system 1T-$TaS_{2-x}Se_x$.

[35] Liguo Ma, Cun Ye, Yijun Yu, Xiu Fang Lu, Xiaohai Niu, Sejoong Kim, Donglai Feng, David Tománek, Young-Woo Son, Xian Hui Chen, and Yuanbo Zhang. A metallic mosaic phase and the origin of mott-insulating state in 1T-TaS_2. *Nature communications*, 7:10956, March 2016.

[36] Jeffrey M. McMahon, Miguel A. Morales, Carlo Pierleoni, and David M. Ceperley. The properties of hydrogen and helium under extreme conditions. *Reviews of Modern Physics*, 84(4):1607–1653, October 2012.

[37] W. L. McMillan. Theory of discommensurations and the commensurate-incommensurate charge-density-wave phase transition. *Phys. Rev. B*, 14:1496–1502, Aug 1976.

[38] Koichi Momma and Fujio Izumi. *VESTA3* for three-dimensional visualization of crystal, volumetric and morphology data. *Journal of Applied Crystallography*, 44(6):1272–1276, Dec 2011.

[39] Kazuo Nakanishi and Hiroyuki Shiba. Domain-like incommensurate charge-density-wave states and the first-order incommensurate-commensurate transitions in layered tantalum dichalcogenides. i. 1T-polytype. *Journal of the Physical Society of Japan*, 43(6):1839–1847, 1977.

[40] Kazuo Nakanishi, Hiroshi Takatera, Yasusada Yamada, and Hiroyuki Shiba. The nearly commensurate phase and effect of harmonics on the successive phase transition in 1T-TaS_2. *Journal of the Physical Society of Japan*, 43(5):1509–1517, 1977.

[41] K. S. Novoselov, A. K. Geim, S. V. Morozov, D. Jiang, Y. Zhang, S. V. Dubonos, I. V. Grigorieva, and A. A. Firsov. Electric field effect in atomically thin carbon films. *Science*, 306(5696):666–669, 2004.

[42] K. S. Novoselov, A. Mishchenko, A. Carvalho, and A. H. Castro Neto. 2d materials and van der waals heterostructures. *Science*, 353(6298), 2016.

[43] Jae Whan Park, Gil Young Cho, Jinwon Lee, and Han Woong Yeom. Emergent honeycomb network of topological excitations in correlated charge density wave. *Nature Communications*, 10:4038, September 2019.

[44] Jiwoong Park, Y. H. Ahn, and Carlos Ruiz-Vargas. Imaging of photocurrent generation and collection in single-layer graphene. *Nano Letters*, 9(5):1742–1746, 2009. PMID: 19326919.

[45] R. E. Peierls. *Quantum Theory of Solids*. Oxford University Press, 2001.

[46] Feng Peng, Ying Sun, Chris J. Pickard, Richard J. Needs, Qiang Wu, and Yanming Ma. Hydrogen clathrate structures in rare earth hydrides at high pressures: Possible route to room-temperature superconductivity. *Phys. Rev. Lett.*, 119:107001, Sep 2017.

[47] Feng Peng, Ying Sun, Chris J. Pickard, Richard J. Needs, Qiang Wu, and Yanming Ma. Hydrogen clathrate structures in rare earth hydrides at high pressures: Possible route to room-temperature superconductivity. *Phys. Rev. Lett.*, 119:107001, Sep 2017.

[48] T. Ritschel, H. Berger, and J. Geck. Stacking-driven gap formation in layered 1t-tas_2. *Phys. Rev. B*, 98:195134, Nov 2018.

[49] K Rossnagel. On the origin of charge-density waves in select layered transition-metal dichalcogenides. *Journal of Physics: Condensed Matter*, 23(21):213001, may 2011.

[50] Andreas Schilling, Marco Cantoni, J. Guo, and H. Ott. Superconductivity above 130 k in the hg-ba-ca-cu-o system. *Nature*, 363:56–58, 05 1993.

[51] C. B. Scruby, P. M. Williams, and G. S. Parry. The role of charge density waves in structural transformations of 1T-TaS_2. *The Philosophical Magazine: A Journal of Theoretical Experimental and Applied Physics*, 31(2):255–274, 1975.

[52] Toshihiro Shimada, Fumio S. Ohuchi, and Bruce A. Parkinson. Work function and photothreshold of layered metal dichalcogenides. *Japanese Journal of Applied Physics*, 33(Part 1, No. 5A):2696–2698, may 1994.

[53] Balazs Sipos, A Kusmartseva, Ana Akrap, Helmuth Berger, L Forró, and Eduard Tutis. From mott state to superconductivity in-1T-TaS_2. *Nature materials*, 7:960–5, 01 2009.

[54] Elliot Snider, Nathan Dasenbrock-Gammon, Raymond McBride, Mathew Debessai, Hiranya Vindana, Kevin Vencatasamy, Keith V Lawler, Ashkan Salamat, and Ranga P Dias. Room-temperature superconductivity in a carbonaceous sulfur hydride. *Nature*, 586(7829):373—377, October 2020.

[55] Albert Spijkerman, Jan L. de Boer, Auke Meetsma, Gerrit A. Wiegers, and Sander van Smaalen. X-ray crystal-structure refinement of the nearly commensurate phase of 1T-TaS_2 in $(3+2)$-dimensional superspace. *Phys. Rev. B*, 56:13757–13767, Dec 1997.

[56] Quirin Stahl, Maximilian Kusch, Florian Heinsch, Gaston Garbarino, Norman Kretzschmar, Kerstin Hanff, Kai Rossnagel, Jochen Geck, and Tobias Ritschel. Collapse of layer dimerization in the photo-induced hidden state of 1T-TaS_2. *Nature Communications*, 11:1247, March 2020.

[57] Ernst Stelzer. *Designing a Confocal Fluorescence Microscope*, pages 33–51. 01 1994.

[58] T. Takahashi, H. Tokailin, and T. Sagawa. Angle-resolved ultraviolet photoelectron spectroscopy of the unoccupied band structure of graphite. *Phys. Rev. B*, 32:8317–8324, Dec 1985.

[59] R. E. Thomson, B. Burk, A. Zettl, and John Clarke. Scanning tunneling microscopy of the charge-density-wave structure in 1T-TaS_2. *Phys. Rev. B*, 49:16899–16916, Jun 1994.

[60] Robert E. Thorne. Charge-density-wave conductors. *Physics Today*, 49(5):42–47, 1996.

[61] Michael Tinkham. *Introduction to Superconductivity*. McGraw-Hill, second edition, 1996.

[62] Adam Tsen, Fabio Cicoira, George Malliaras, and Jiwoong Park. Photoelectrical imaging and characterization of point contacts in pentacene thin-film transistors. *Applied Physics Letters - APPL PHYS LETT*, 97, 07 2010.

[63] Adam Tsen, Luke Donev, Huseyin Kurt, Lihong Herman, and Jiwoong Park. Imaging the electrical conductance of individual carbon nanotubes with photothermal current microscopy. *Nature nanotechnology*, 4:108–13, 03 2009.

[64] Adam W. Tsen, Robert Hovden, Dennis Wang, Young Duck Kim, Junichi Okamoto, Katherine A. Spoth, Yu Liu, Wenjian Lu, Yuping Sun, James C. Hone, Lena F. Kourkoutis, Philip Kim, and Abhay N. Pasupathy. Structure and control of charge density waves in two-dimensional TaS_2. *Proceedings of the National Academy of Sciences*, 112(49):15054–15059, 2015.

[65] S. Uchida, K. Tanabe, and S. Tanaka. Nonlinear conduction in two-dimensional cdw system: 1T-TaS_2. *Solid State Communications*, 27(6):637–640, 1978.

[66] Igor Vaskivskyi, Jan Gospodaric, Serguei Brazovskii, Damjan Svetin, Petra Sutar, Evgeny Goreshnik, Ian A. Mihailovic, Tomaz Mertelj, and Dragan Mihailovic. Controlling the metal-to-insulator relaxation of the metastable hidden quantum state in 1T-TaS_2. *Science Advances*, 1(6), 2015.

[67] Igor Vaskivskyi, I. Mihailovic, S. Brazovskii, Jan Gospodaric, T. Mertelj, Damjan Svetin, Petra Šutar, and Dragan Mihailovic. Fast electronic resistance switching involving hidden charge density wave states. *Nat Commun*, 7, 05 2016.

[68] Igor Vaskivskyi, I. Mihailovic, S. Brazovskii, Jan Gospodaric, T. Mertelj, Damjan Svetin, Petra Šutar, and Dragan Mihailovic. Fast electronic resistance switching involving hidden charge density wave states. *Nat Commun*, 7, 05 2016.

[69] Hui Wang, John S. Tse, Kaori Tanaka, Toshiaki Iitaka, and Yanming Ma. Superconductive sodalite-like clathrate calcium hydride at high pressures. *Proceedings of the National Academy of Sciences*, 109(17):6463–6466, 2012.

[70] L. Wang, I. Meric, P. Y. Huang, Q. Gao, Y. Gao, H. Tran, T. Taniguchi, K. Watanabe, L. M. Campos, D. A. Muller, J. Guo, P. Kim, J. Hone, K. L. Shepard, and C. R. Dean. One-dimensional electrical contact to a two-dimensional material. *Science*, 342(6158):614–617, 2013.

[71] Y. D. Wang, W. L. Yao, Z. Xin, T. Han, Z. G. Wang, L. Chen, C. Cai, Y. Li, and Y. Zhang. Band insulator to mott insulator transition in 1t-tas2. *Nature Communications*, 11, 2020.

[72] J.A. Wilson, F.J. Di Salvo, and S. Mahajan. Charge-density waves and superlattices in the metallic layered transition metal dichalcogenides. *Advances in Physics*, 24(2):117–201, 1975.

[73] Xian Wu and Charles Lieber. Direct observation of growth and melting of the hexagonal-domain charge-density-wave phase in 1T-TaS_2 by scanning tunneling microscopy. *Physical review letters*, 64:1150–1153, 04 1990.

[74] Xian Liang Wu and Charles M. Lieber. Hexagonal domain-like charge density wave phase of TaS_2 determined by scanning tunneling microscopy. *Science*, 243(4899):1703–1705, 1989.

[75] Masaro Yoshida, Ryuji Suzuki, Yijin Zhang, Masaki Nakano, and Yoshihiro Iwasa. Memristive phase switching in two-dimensional 1T-TaS_2 crystals. *Science Advances*, 1(9), 2015.

[76] Yijun Yu, F. Yang, X. F. Lu, Y. Yan, Yong-Heum Cho, L. Ma, X. Niu, S. Kim, Y. Son, D. Feng, S. Li, S. Cheong, X. Chen, and Y. Zhang. Gate-tunable phase transitions in thin flakes of 1T-TaS_2. *Nature nanotechnology*, 10 3:270–6, 2015.

[77] Weijie Zhao, Zohreh Ghorannevis, Leiqiang Chu, Minglin Toh, Christian Kloc, Ping-Heng Tan, and Goki Eda. Evolution of electronic structure in atomically thin sheets of WS_2 and WSe_2. *ACS nano*, 7, 12 2012.

[78] P. J. Zomer, M. H. D. Guimarães, J. C. Brant, N. Tombros, and B. J. van Wees. Fast pick up technique for high quality heterostructures of bilayer graphene and hexagonal boron nitride. *Applied Physics Letters*, 105(1):013101, 2014.

APPENDICES

Appendix A

Atomic Force Microscopy of 2-D hetero-structures

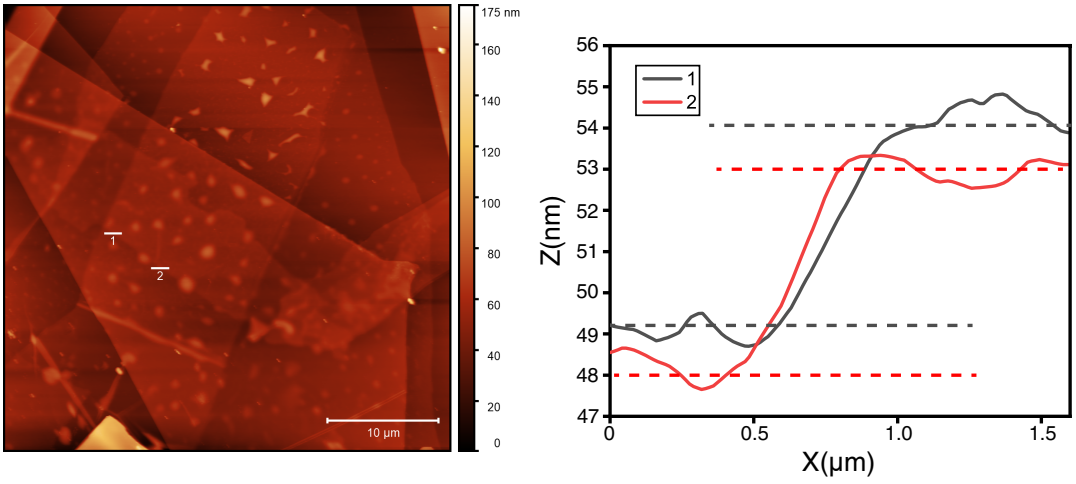

Figure A.1: AFM image of device in Fig 4.3

2-D van-der-waals materials conform over each other in a vertical hetero-structure geometry. This allows for measurement of 1T-TaS_2 flake thickness underneath a relatively

thicker h-BN with a good precision. Fig A.1 shows the AFM image of the device in Fig 4.3. Line cuts 1 and 2 along the 1T-TaS_2 edge show that the flake thickness is 5nm.

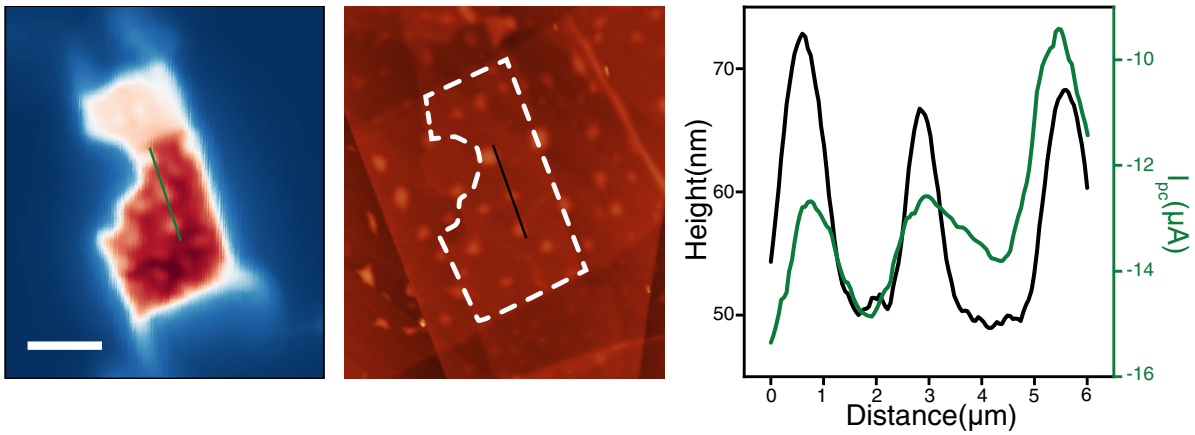

Figure A.2: Comparison between photocurrent (left) and atomic force microscopy (middle) images of device shown in Fig 4.3 show close correspondence between the spot-like photocurrent features and physical bumps, which could be attributed to bubbles or unwanted particles trapped at the interface between layers. Scale bar is 5 μm. Line profiles are further shown on the right.

Appendix B

Photocurrent Imaging of 1T-TaS_2 in lateral geometry

A lateral geometry consisting of a 22-nm 1T-TaS_2 flake (with a thinner end) contacted by 2 Au electrodes and capped by h-BN is a simpler heterostructure to assemble. The photocurrent generation is dominated by the Seebeck effect between Au/1T-TaS_2 and is thus localized near the contact regions. The polarity of photocurrent changes between NC and C phase in a reversible manner. B.1 This can be explained by the change of polarity of majority carriers [26] across the NC-C transition. While some form of intermediate states are observed during the transition temperatures the features are not directly interpretable.

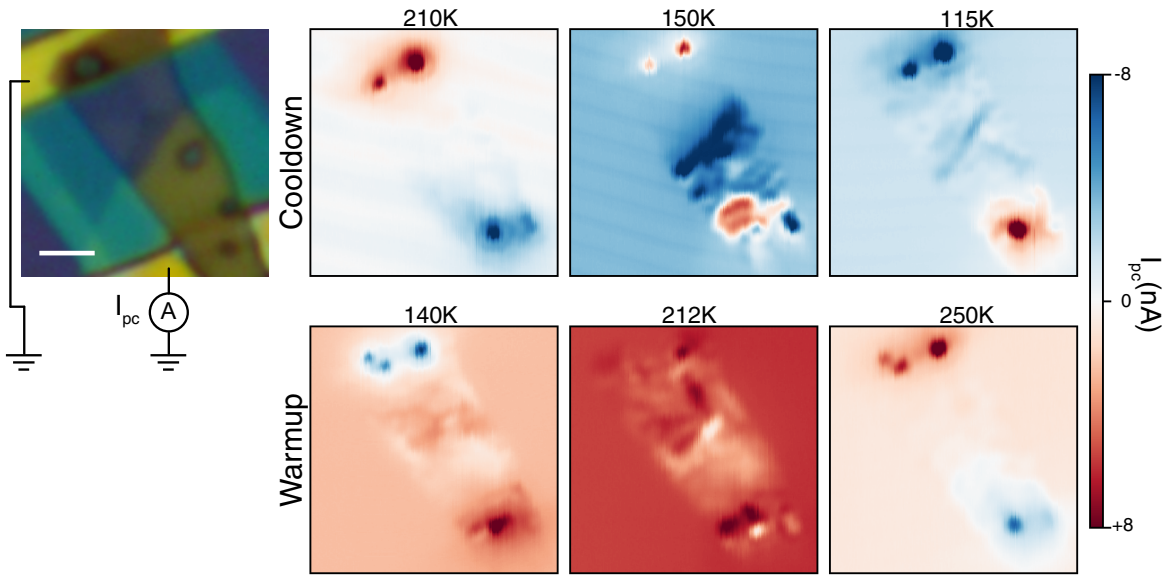

Figure B.1: Photocurrent images of a 1T-TaS_2 device in a lateral geometry for different temperatures across the NC-C transition during cool-down(top) and warm-up(bottom).The left panel shows the measurement geometry overlaid on the optical image. Scale bar is $5\mu m$.